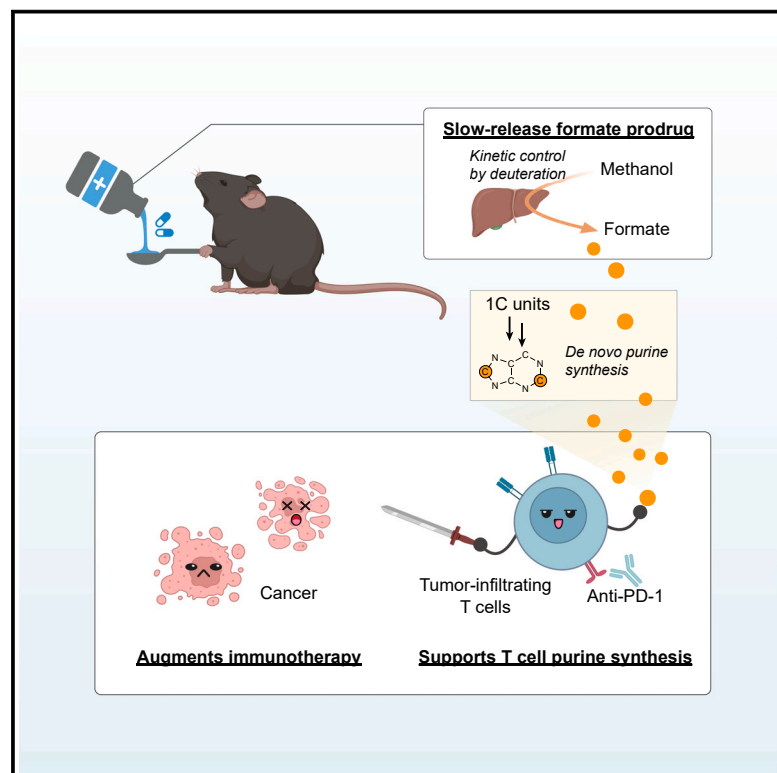


Cell Chemical Biology

One-carbon unit supplementation fuels purine synthesis in tumor-infiltrating T cells and augments checkpoint blockade

Graphical abstract



Authors

Xincheng Xu, Zihong Chen,
Caroline R. Bartman, Xi Xing,
Kellen Olszewski,
Joshua D. Rabinowitz

Correspondence

kolszews@princeton.edu (K.O.),
josh@princeton.edu (J.D.R.)

In brief

Immune checkpoint blockade has revolutionized cancer treatment yet still fails many patients. Xu, Chen, Olszewski et al. show that tumor-infiltrating T cells require one-carbon (1C) units for purine synthesis and that pharmacological 1C supplementation can overcome metabolic barriers to anti-cancer immunity, leading to durable tumor regressions with checkpoint blockade.

Highlights

- Isotope tracing and cell sorting reveal cell type-specific nucleotide sources *in vivo*
- Both MC38 cancer cells and tumor-infiltrating T cells synthesize purines *de novo*
- Formate supplementation supports purine synthesis in tumor-infiltrating T cells
- Methanol acts as a formate prodrug and augments anti-PD-1 efficacy



Article

One-carbon unit supplementation fuels purine synthesis in tumor-infiltrating T cells and augments checkpoint blockade

Xincheng Xu,^{1,2,3,4} Zihong Chen,^{1,2,3,4} Caroline R. Bartman,^{1,2,3} Xi Xing,^{1,2,3} Kellen Olszewski,^{3,4,*} and Joshua D. Rabinowitz^{1,2,3,5,*}

¹Department of Chemistry, Princeton University, Princeton, NJ, USA

²Lewis-Sigler Institute for Integrative Genomics, Princeton University, Princeton, NJ, USA

³Ludwig Institute for Cancer Research, Princeton Branch, Princeton University, Princeton, NJ, USA

⁴These authors contributed equally

⁵Lead contact

*Correspondence: kolszews@princeton.edu (K.O.), joshhr@princeton.edu (J.D.R.)

<https://doi.org/10.1016/j.chembiol.2024.04.007>

SUMMARY

Nucleotides perform important metabolic functions, carrying energy and feeding nucleic acid synthesis. Here, we use isotope tracing-mass spectrometry to quantitate contributions to purine nucleotides from salvage versus *de novo* synthesis. We further explore the impact of augmenting a key precursor for purine synthesis, one-carbon (1C) units. We show that tumors and tumor-infiltrating T cells (relative to splenic or lymph node T cells) synthesize purines *de novo*. Shortage of 1C units for T cell purine synthesis is accordingly a potential bottleneck for anti-tumor immunity. Supplementing 1C units by infusing formate drives formate assimilation into purines in tumor-infiltrating T cells. Orally administered methanol functions as a formate pro-drug, with deuteration enabling kinetic control of formate production. Safe doses of methanol raise formate levels and augment anti-PD-1 checkpoint blockade in MC38 tumors, tripling durable regressions. Thus, 1C deficiency can gate antitumor immunity and this metabolic checkpoint can be overcome with pharmacological 1C supplementation.

INTRODUCTION

Cancer metabolism was revitalized early this century by aspirations to cut off the tumor fuel supply. Intensive research efforts explored central carbon pathways feeding both energy and biosynthetic metabolism.^{1,2} Identification of alternative nutrient acquisition routes based on nutrient scavenging,^{3,4} such as micropinocytosis,^{5,6} enriched the field but complicated efforts to starve tumor cells, and up to now there has been no clinical success in targeting central metabolism for cancer therapy.

With the rise of immunotherapy, an alternative opportunity emerged: to remove metabolic barriers to successful antitumor immune response.⁷ A myriad of such potential barriers have been identified, including intratumoral competition for glucose,^{8–10} amino acids,^{11,12} and oxygen,^{13,14} and potential metabolic impairment of immune cells by cancer cell-derived products like lactate or kynurenine,^{15,16} with inhibitors of kynurenine synthesis entering the clinic but showing limited benefits in human patients.¹⁷

Historically, the most therapeutically impactful area of cancer and immune metabolism, dating back to Sydney Farber,¹⁸ regards nucleotide metabolism, including folate enzymes that generate one-carbon (1C) units required for purine and thymidine synthesis.¹⁹ Inhibitors of nucleotide metabolism are both anti-

cancer agents and immunosuppressants. Anti-purines such as azathioprine, 6-mercaptopurine, and 6-thioguanine are frequently used in the treatment of autoimmune disease.²⁰ Methotrexate, which targets the production by dihydrofolate reductase of the biologically active form of folate, tetrahydrofolate (THF), is a first-line agent for T cell leukemia and rheumatoid arthritis.^{21,22} The clinical importance of these agents as immunosuppressants argues for purine biosynthetic capacity being a key determinant of immune response.

De novo purine synthesis starts with glutamine-mediated amination of phosphoribosyl pyrophosphate (PRPP), followed by a series of steps incorporating glycine and two folate-bound 1C units, in the form of formyl-tetrahydrofolate (formyl-THF). The 1C unit in THF can come from multiple precursors, including serine or free circulating formate. Activated T cells upregulate *de novo* serine synthesis and the mitochondrial enzymes catalyzing conversion of serine into formyl-THF: SHMT2 and MTHFD2.²³ Impairment of MTHFD2 leads to failure of effector T cell function and a shift toward a suppressor state.²⁴ Mitochondrial formyl-THF is exported to the cytosol as free formate, which together with formate imported from circulation, gets converted by MTHFD1 to cytosolic formyl-THF fueling *de novo* purine synthesis. CD8⁺ T cells with the loss of *Mthfd1* are strongly depleted



in tumors and spleen, supporting the important role of cytosolic formate incorporation for anti-tumor immunity.²⁵

The product of *de novo* purine synthesis is inosine monophosphate (IMP), which can be converted in two steps into either AMP or guanosine monophosphate (GMP). These purines can also be synthesized via salvage pathways, by reaction of hypoxanthine, adenine, or guanine with PRPP to yield IMP, AMP, or GMP. Further phosphorylation yields the key energy molecules and nucleic acid precursors ATP and guanosine triphosphate (GTP). While the nucleobases hypoxanthine, adenine, and guanine are the direct substrates for purine salvage, their corresponding nucleosides (inosine, adenosine, and guanosine) may also be major players in the inter-organ exchange of purines.^{26–28} Inborn errors in nucleoside metabolism manifest as severe combined immunodeficiency.^{29–31} Inosine is a component of an immune booster used in some viral infections (inosine pranobex)^{32,33} and has been suggested to be a microbiome-derived product that supports cancer immunotherapy efficacy.³⁴

Here we investigate the relative contributions of *de novo* and salvage purine synthesis to the key purine end product ATP, in normal tissues, bulk MC38 tumors, splenic and lymph node CD8⁺ T cells, and tumor-infiltrating CD8⁺ T cells (TILs). We find that MC38 tumors and TILs synthesize a particularly high fraction of their ATP purine ring *de novo*. We further show that both serine and free circulating formate provide 1C units to support TIL purine synthesis, and that pharmacological boosting of circulating formate by administering methanol as a formate prodrug enhances anti-PD-1 immunotherapy.

RESULTS

Abundances of circulating purines

We began by establishing isotope-tracing methods for the source of the purine ring in ATP and GTP *in vivo*. Serine is an established tracer for *de novo* purine synthesis, which feeds into the ring by generating 1C units and glycine, which together account for 4 of the 5 carbon atoms in purines (Figure 1A). Infusion of [U-¹³C]serine accordingly probes *de novo* purine production.^{35,36}

Methods for measuring salvage synthesis were less well established. We began by carefully measuring the circulating concentrations of the potential salvage substrates. These measurements were technically complicated by the propensity for these low-energy metabolites to be rapidly produced by nucleotide degradation. For example, inosine and hypoxanthine concentrations in the tail blood were several-fold higher than in the arterial blood (which was sampled noninvasively from pre-catheterized mice) (Figure S1A). Moreover, when blood was allowed to sit on ice, while most metabolite concentrations did not change, inosine and hypoxanthine increased greatly (Figures 1B–1C, and S1B). Measurements from quickly processed arterial serum showed undetectable purine nucleotides, and that inosine and adenosine are the most abundant circulating purines (and uridine, cytidine, and thymidine are the most abundant circulating pyrimidines, Figure 1D). Accordingly we focused on inosine and adenosine as tracers.

Circulatory fluxes of nucleosides

We measured these nucleosides' circulatory turnover flux (i.e., whole-body rate of release of these metabolites into the circula-

tion, or "rate of appearance," Figure 1E) by infusing them in ¹⁵N-labeled form (Figure 1F). This required continued care, as otherwise the labeling was diluted by unphysiological production during sampling (Figures 1B and S1B–S1D). We found that inosine and adenosine have much higher circulating fluxes than pyrimidine nucleosides (Figure 1G).

[U-¹⁵N]inosine infusion labeled allantoin (a terminal purine degradation product, which plays a similar role in mouse to uric acid in human), to a similar extent as inosine itself (Figure S1D). As allantoin labeling is insensitive to sampling method and sample handling (Figures S1D and S1E), we used its labeling as a surrogate for circulating inosine in subsequent experiments. Labeling of adenosine from inosine was limited (Figure S1F), but not vice versa (Figure S1G). This is consistent with inosine feeding into tissue nucleotides directly, whereas adenosine can contribute both directly and indirectly via circulating inosine, which can be produced from adenosine via the ubiquitous and irreversible adenosine deaminase (ADA) reaction.

Tumors synthesize purines *de novo*

We next explored the contributions of *de novo* synthesis ([U-¹³C]serine tracer) and salvage ([U-¹⁵N]inosine and [U-¹⁵N]adenosine tracers) to tissue and MC38 murine colon cancer tumor purines by infusing these tracers for 13 h (Figure 1A). The long infusion is necessary for reaching isotopic pseudo-steady state due to the slow turnover of the purine skeleton relative to large tissue purine pools (Figure S1H). The infusion modestly increases serum serine with a similar non-significant trend also for circulating purines (Figures S1I and S1J). While labeling differed depending on the tracer and target tissue, using either serine or inosine as the tracer, different purine nucleotides (IMP, AMP, ADP, ATP, GMP, and guanosine diphosphate [GDP]) generally labeled to a similar extent, consistent with both serine and inosine entering all purines via the common precursor IMP (Figures S1K and S1L). In contrast, in a subset of tissues, adenosine labeled adenosine nucleotides preferentially over guanosine nucleotides (Figure S1M). This reflects direct assimilation of adenosine without its prior conversion to IMP, as all five nitrogen atoms were retained (one is lost when adenosine becomes inosine) (Figure S1N).

Because it is the most abundant purine, we focused on ATP as the most convenient readout. Inosine salvage, adenosine salvage, and *de novo* synthesis from serine each were the primary ATP purine ring contributors in certain tissues (Figure 1H). For example, *de novo* synthesis predominated in intestine; salvage from inosine in pancreas, kidney, and spleen; and salvage from adenosine in lung. In MC38 tumors, *de novo* synthesis predominated.

De novo purine synthesis in TILs versus splenic and lymph node T cells

Tumors and organs are heterogeneous.³⁷ Given the importance of CD8⁺ T cells to anticancer immunity,³⁸ we were particularly curious about the sources of purines in CD8⁺ T cells from tumors, spleen, and tumor-draining lymph nodes (TDLNs). In both tumors and lymphoid organs (thymus and spleen), most salvage synthesis was from inosine (Figure 1H). Accordingly, we focused on comparing tracing from serine versus inosine.

Using [U-¹³C]serine and [U-¹⁵N]inosine, ATP derived from serine versus inosine separate based on exact mass, allowing

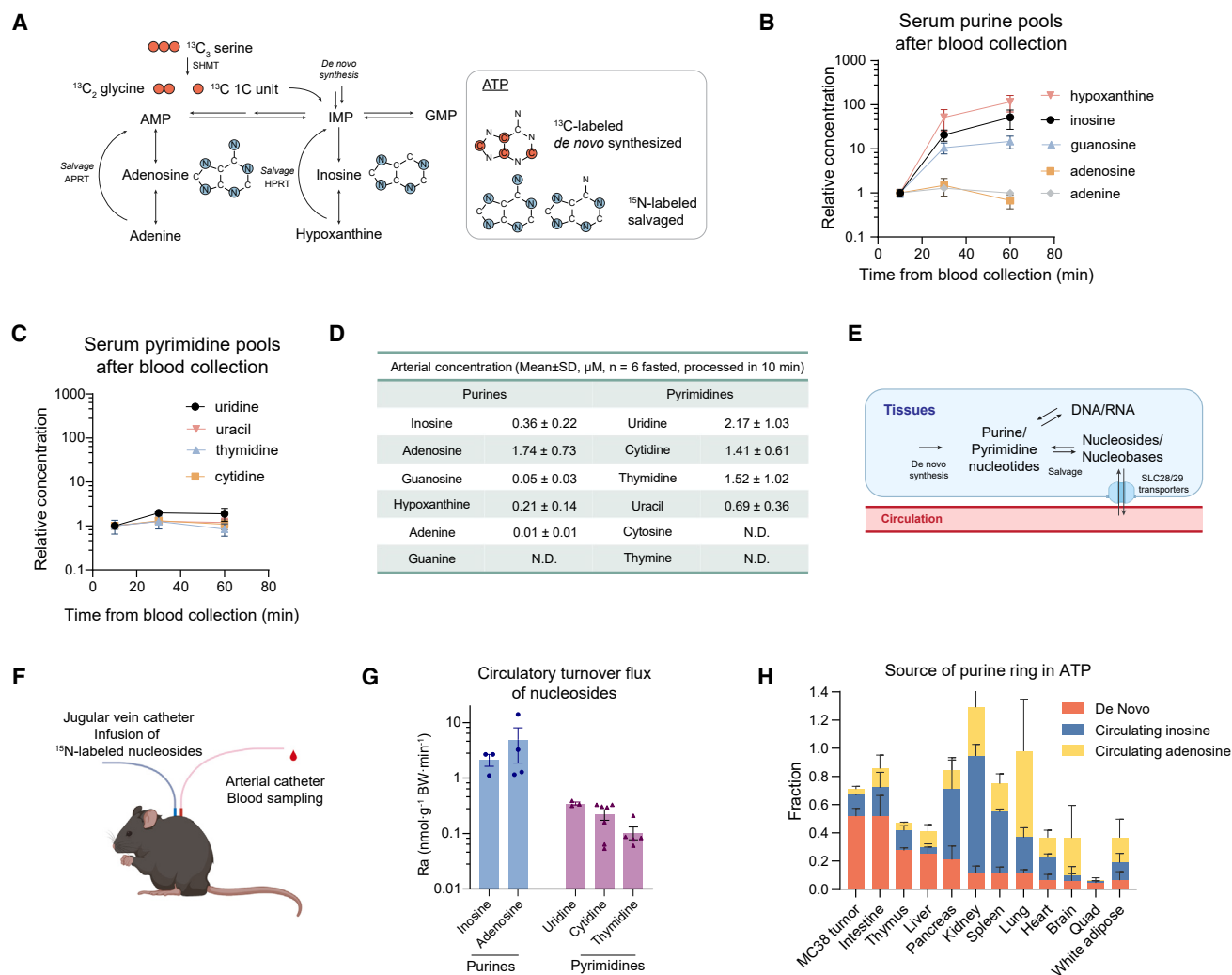


Figure 1. Source of ATP's purine ring in tissues and tumors

(A) Schematic of tracing purine *de novo* synthesis and salvage using [U- 13 C]serine, [U- 15 N]inosine, and [U- 15 N]adenosine.

(B) Serum concentrations of certain purine nucleosides and bases rise when isolated blood sits on ice ($n = 3$).

(C) Serum concentrations of pyrimidine nucleosides and bases are relatively stable when isolated blood sits on ice ($n = 3$).

(D) Concentrations of purine and pyrimidine species in quickly processed arterial serum from fasted mice ($n = 6$). Blood was kept on ice after sampling. Serum was isolated by centrifugation and extracted in 10 min from sample collection. N.D., non-detectable.

(E) Schematic diagram of nucleoside/nucleotide metabolism.

(F) Schematic of measuring circulatory turnover flux (rate of appearance) of nucleosides in mice.

(G) Circulatory turnover flux of purine and pyrimidine nucleosides. $n = 3$ for inosine; $n = 4$ for adenosine; $n = 5$ for uridine and thymidine; $n = 6$ for cytidine.

(H) Contribution to ATP's purine ring over 13 h tracer infusions by *de novo* synthesis ($n = 3$) and salvage of circulating inosine ($n = 3$) and adenosine ($n = 3$) in each tissue. Quad, quadriceps femoris muscle. Unlabeled ATP reflects incomplete purine turnover during the infusion duration or production from other sources, likely primarily nucleic acid degradation. Mean \pm SD except for mean \pm SEM in (G); n indicates the number of male mice. See also Figure S1.

both tracers to be used in parallel in the same mouse. To isolate CD8 $^{+}$ T cells from mice receiving the dual tracers, we first dissociated normal spleen, MC38 tumors, and tumor-draining inguinal lymph nodes to single cells, followed by magnetic activated cell sorting (MACS) (Figure 2A). The CD8 $^{+}$ enriched and depleted populations were sampled for flow cytometry validation (Figures S2A and S2B), and the rest were placed directly into organic solvent to quench metabolism (Figure 2A).

A key challenge in analyzing metabolic heterogeneity is the propensity for metabolite levels and labeling to change during cell handling and purification.^{39–41} To evaluate this, we collected the

single cell suspension right before MACS and compared metabolomics and labeling to directly quenched tumor and spleen specimens. The purification process substantially altered the concentrations of most metabolites, including serine and glycine (Figures S2C and S2D). It also diluted their labeling greatly (more than 2-fold) (Figures S2E and S2F), reflecting their production, likely from protein catabolism during the purification process (further evidenced by increased leucine and isoleucine, Figure S2C). ATP labeling also declined significantly, but 75% of the labeled fraction was retained (Figure 2B). The substantial retention of ATP labeling fraction reflects ATP being a high abundance

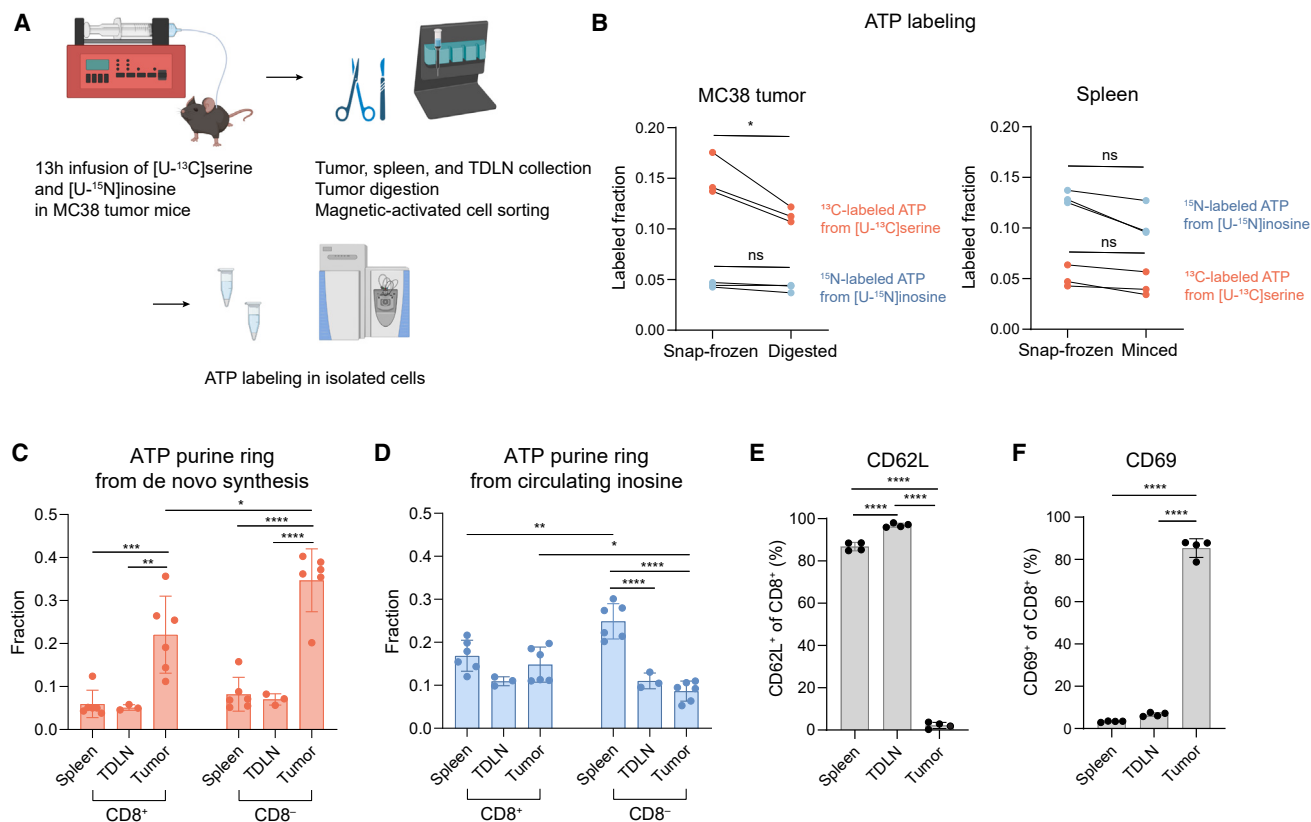


Figure 2. CD8⁺ TILs carry out more *de novo* purine synthesis than splenic CD8⁺ T cells

(A) Experimental schema of tracing ATP source in different cell populations. Following 13-h infusion of both [U-¹³C]serine and [U-¹⁵N]inosine (simultaneously) in mice bearing MC38 tumors, tumors were dissociated into single-cell suspensions. The CD8⁺ and CD8⁻ populations were fractionated by magnetic-activated cell sorting, and ATP labeling was measured by LC-MS.

(B) The preservation of ATP labeling (from [U-¹³C]serine and [U-¹⁵N]inosine infusion) after tissue dissociation compared to the same sample being snap-frozen ($n = 3$ males). p values were calculated by paired two-tailed Student's t test.

(C and D) Fraction of ATP's purine ring from (C) *de novo* synthesis versus (D) circulating inosine in CD8⁺ or CD8⁻ populations in MC38 tumor ($n = 6$, with 3 males and 3 females), tumor-draining inguinal lymph node (TDLN, $n = 3$ females), and spleen ($n = 6$, with 3 males and 3 females). p values were calculated by one-way ANOVA with Tukey test for multiple comparisons.

(E and F) Frequency of (E) CD62L⁺ and (F) CD69⁺ cells among CD8⁺ T cells from MC38 tumor, tumor-draining inguinal lymph node, and spleen ($n = 4$ females). p values were calculated by one-way ANOVA with Tukey test for multiple comparisons. Mean \pm SD in (C–F). n indicates the number of mice. ns, $p > 0.05$; * $p < 0.05$; ** $p < 0.01$; *** $p < 0.001$; **** $p < 0.0001$. See also Figure S2.

metabolite that cannot be readily produced during the nutrient-poor conditions of cell isolation. Notably, ATP catabolism will not alter the labeling pattern of the residual ATP. Thus, we were able to use ATP labeling from sorted cells to identify the extent of *de novo* versus salvage synthesis as the source of purines.

Purine sources were strikingly different between CD8⁺ TILs and those T cells from spleen and TDLNs. The splenic and TDLN CD8⁺, like spleen, both had much higher fraction of purine labeling from inosine (salvage) than serine (*de novo*). Conversely, the TILs had much higher purine labeling from serine than inosine. The upregulated purine fraction from serine in CD8⁺ TILs distinguished them from T cells in secondary lymphoid organs (Figures 2C and 2D). Thus, CD8⁺ T cells within tumors stand out for high *de novo* purine synthesis.

We hypothesized that activation contributed to the distinct purine source profile in TILs. Applying our dual-tracer strategy to cultured CD8⁺ T cells, we indeed observed a shift from salvage to *de novo* synthesis as the predominant purine source following

in vitro activation (Figures S2G and S2H). Further analysis of naive (CD62L) and activation (CD69) marker expression across CD8⁺ populations was consistent with our hypothesis: in contrast to splenic and TDLN CD8⁺ which are mostly naive T cells, the majority of CD8⁺ from tumors are activated (Figures 2E and 2F). Thus, activation likely drives the elevated *de novo* purine synthesis in TILs.

Both serine and circulating formate contribute to tumor 1C units

Having established a high *de novo* contribution to purines in tumors and TILs, we next sought to understand the sources of the 1C units supporting purine synthesis in these contexts (Figure 3A). Two important ones are serine's hydroxymethyl carbon and formate. Accordingly, we infused MC38 tumor-bearing mice with [U-¹³C]serine or [¹³C]formate for 13 h and measured ATP labeling. MC38 tumor ATP was labeled substantially by both tracers (Figure 3B).

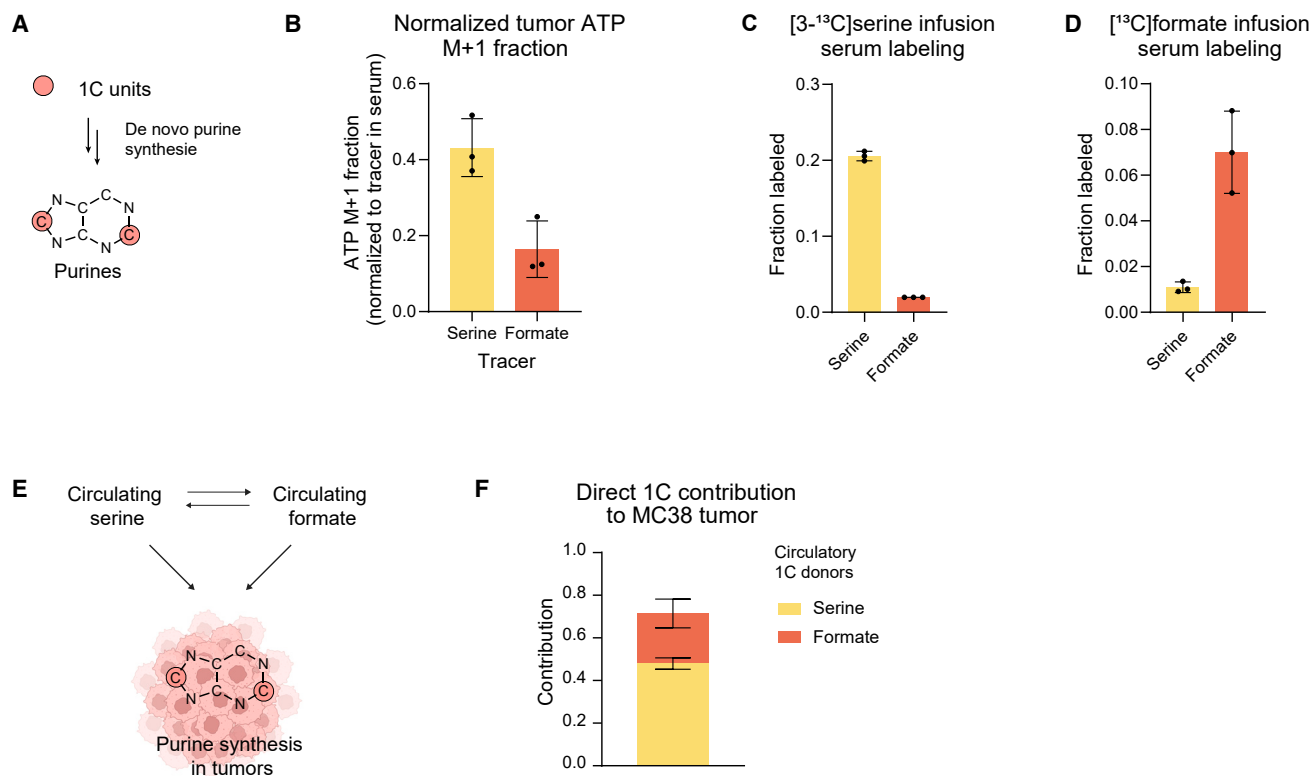


Figure 3. MC38 tumors synthesize purines *de novo* with 1C units from serine and circulating formate

(A) Schematic of 1C unit incorporation into the purine ring via *de novo* purine synthesis.

(B) ATP M+1 labeled fraction in MC38 tumor, normalized to serum tracer enrichment for [U-¹³C]serine and [¹³C]formate infusions ($n = 3$).

(C and D) Circulating serine and formate labeling in (C) [^{3-¹³C}]serine or (D) [¹³C]formate infusions ($n = 3$).

(E) Schematic representation of the potential for serine and formate to interconvert or directly feed tumor 1C units.

(F) Direct contribution of circulating serine and formate to 1C units in MC38 tumor, determined by linear algebra with data from (B–D). Mean \pm SD in (B–D). Mean \pm SEM in (F). n indicates the number of male mice. See also Figure S3.

Formate was only slightly labeled from serine (Figure 3C), and vice versa (Figure 3D), implying that most circulating formate comes from a source other than serine, perhaps microbiome metabolism. The observed limited cross-labeling between serine and formate suggest that both of their contributions to tumor ATP are largely direct. To quantify these contributions, we recognized that the steady state ATP M+1 fraction, $L_{ATP,M+1}$, is related to 1C unit labeling (L_{1C}) by

$$L_{ATP,M+1} = 2 \cdot f_{de\ novo} \cdot L_{1C} \cdot (1 - L_{1C}) \cong 2f_{de\ novo} L_{1C} \quad (\text{Equation 1})$$

in which $f_{de\ novo}$ is the fraction of ATP from *de novo* synthesis (measured independently in Figure 1H). We further corrected by linear algebra for any cross-labeling (Figure 3E),⁴² to arrive at a direct 1C contribution from each tracer, which was about 2 \times larger for circulating serine than for formate, with the combination accounting for 75% of all tumor purine 1C units (Figure 3F). From the serine tracer, MC38 tumor serine was less labeled than circulating serine, presumably reflecting *de novo* serine synthesis within the tumor (Figure S3A). Correcting for this serine also led to nearly complete accounting for tumor 1C units, roughly 80% from serine and 20% from formate (Figure S3B).

We then carried out similar analysis of purine 1C unit sources from CD8⁺ TILs isolated from these tumors. They also showed a

primary contribution from serine with a meaningful additional contribution from formate (Figure S3C). Thus, both MC38 tumors as a whole and TILs have upregulated *de novo* purine synthesis supported by 1C units coming from serine and circulating formate.

Increasing circulating formate drives its usage by T cells

We hypothesized that formate's contribution to CD8⁺ TIL 1C units is limited by its circulating level (50 μ M in mouse serum). To explore this, we carried out perturbative [¹³C]formate infusions, increasing total serum formate concentrations by up to 6-fold (Figure 4A). In these experiments, endogenously produced formate is unlabeled (M+0) and infused formate is ¹³C₁ (M+1). The perturbative labeled formate infusion led to increased ATP labeling in both CD8⁺ TILs (Figure 4B) and splenic CD8⁺ T cells (Figure 4C). Here, ATP can be unlabeled (reflecting pre-existing purine rings or synthesis from unlabeled substrates like serine), M+1 (reflecting synthesis with a single 1C unit coming from infused labeled formate), or M+2 (reflecting synthesis with both purine 1C units coming from infused labeled formate) (Figure 4D). Quantitatively, the ratio of M+2 to M+1 ATP is determined by the 1C pool labeling fraction (Equation 16 in data analysis). Correcting for the labeled formate fraction in the circulation, the contribution of formate to total purine 1C units

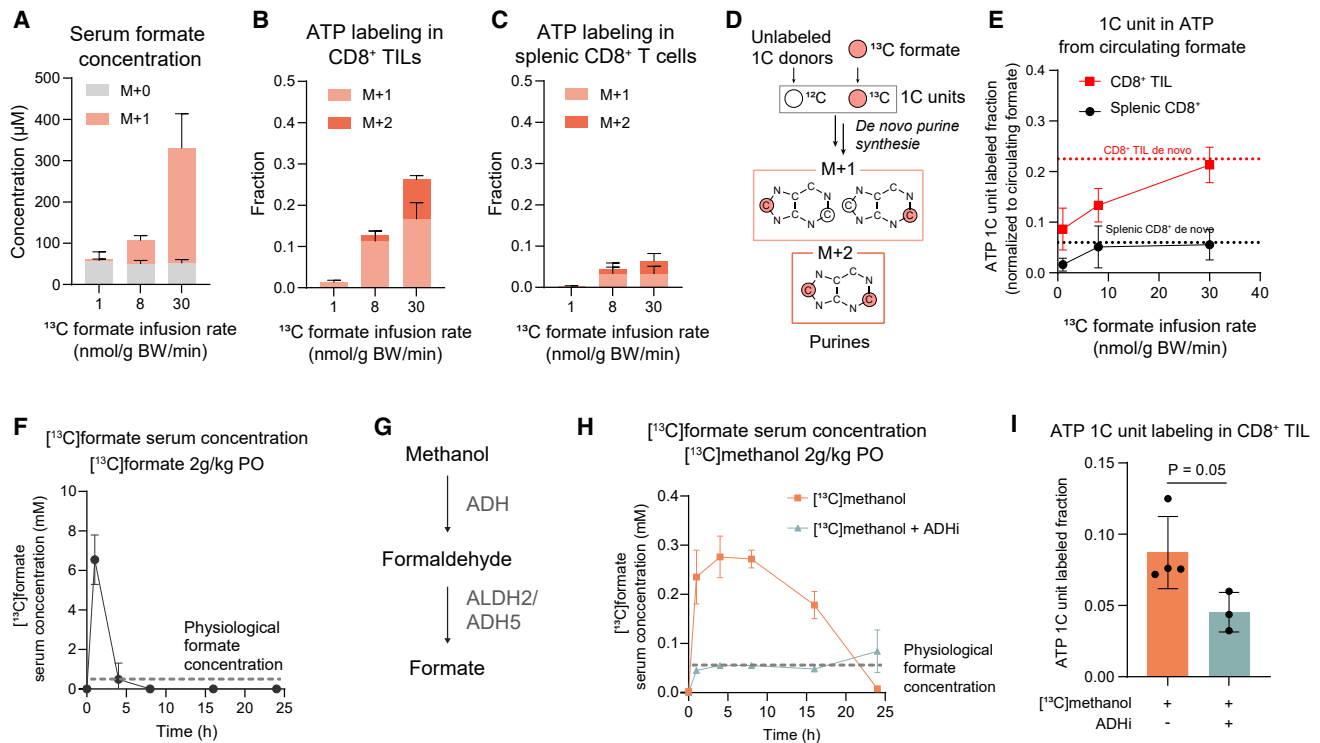


Figure 4. Experimental augmentation of circulating formate drives its usage by CD8⁺ TILs

(A) Circulating formate concentration and labeling achieved by infusing [¹³C]formate at different rates ($n = 3$). (B) Resulting ATP labeling in CD8⁺ TILs ($n = 4$ for 8 nmol/g BW/min; $n = 3$ for others). (C) Resulting ATP labeling in splenic CD8⁺ T cells ($n = 3$ for 1 nmol/g BW/min; $n = 5$ for others). (D) Schematic of 1C unit incorporation into the purine ring via *de novo* purine synthesis, resulting in M+1 and M+2 labeled purines. (E) Relationship between [¹³C]formate infusion rate and circulating formate contribution to total ATP 1C units in CD8⁺ TILs and splenic CD8⁺ T cells. Calculated from data in (A–C). Dashed lines: fractions of purine from *de novo* synthesis (from Figure 2C). (F) Serum [¹³C]formate concentration over time after 2 g/kg [¹³C]formate oral gavage (PO) ($n = 3$). Dashed line: physiological formate concentration. (G) Schematic of methanol metabolism to formate. (H) Serum [¹³C]formate concentration over time after 2 g/kg [¹³C]methanol PO, with ($n = 3$) or without ($n = 5$) ADH inhibitor (fomepizole, 200 mg/kg PO). Dashed line: physiological formate concentration. (I) Labeling of ATP 1C units in CD8⁺ TILs 12 h after 2 g/kg [¹³C]methanol PO with and without ADH inhibitor (fomepizole, 200 mg/kg PO) ($n = 4$ for methanol alone; $n = 3$ for methanol with fomepizole). p values were calculated by two-tailed Student's t test. Mean \pm SD in (F) and (H). Mean \pm SEM in others. n indicates the number of male mice. See also Figure S4.

increased preferentially in the TILs (Figure 4E). Circulating serine labeling was also modestly elevated, but much less than formate or the 1C unit enrichment in CD8⁺ TILs (Figure S4A). Thus, increasing formate availability drives its direct usage in TIL purine synthesis.

As augmentation of CD8⁺ TIL purine synthesis could be beneficial for anti-tumor immunity, we looked for a more convenient way to elevate circulating formate levels. Formate becomes toxic at concentrations in the range of 5–10 mM,⁴³ with pathological formate elevations responsible for the ocular toxicity (blindness) resulting from uncontrolled methanol ingestion. Oral gavage administration of [¹³C]formate (2 g/kg) resulted in a transient increase in circulating formate, which reached potentially toxic levels at 1 h and declined to baseline within 5 h (Figure 4F).

The liver can convert methanol into formate, with methanol itself at least as safe as ethanol, except for its potential to lead to toxic formate accumulation (Figure 4G).⁴⁴ Accordingly, we explored the possibility that oral methanol gavage could be used to produce more stable circulating formate elevations.

[¹³C]methanol (2 g/kg) elevated formate several-fold for over 12 h, while staying more than 10-fold below the concerning formate level of 5 mM (Figure 4H). Such labeled methanol administration was sufficient to contribute substantially to CD8⁺ TIL purine synthesis (Figure 4I). When alcohol dehydrogenase (ADH) is inhibited by fomepizole, both [¹³C]formate production and its incorporation into CD8⁺ TIL decreased (Figures 4H and 4I). Thus, methanol is a formate prodrug that elevates circulating formate concentrations and provides 1C units for TILs.

Methanol supplementation synergizes with checkpoint inhibition

Based on the hypothesis that T cells responding to checkpoint blockade can sometimes be limited by insufficient 1C units (Figure 5A), we next explored the potential for methanol to augment the effectiveness of checkpoint blockade. Mice bearing 100 mm³ MC38 tumors received anti-PD1 antibody (or isotype control) on four occasions over 10 days, with or without daily gavage of methanol 2 g/kg (Figure 5B). In the absence of

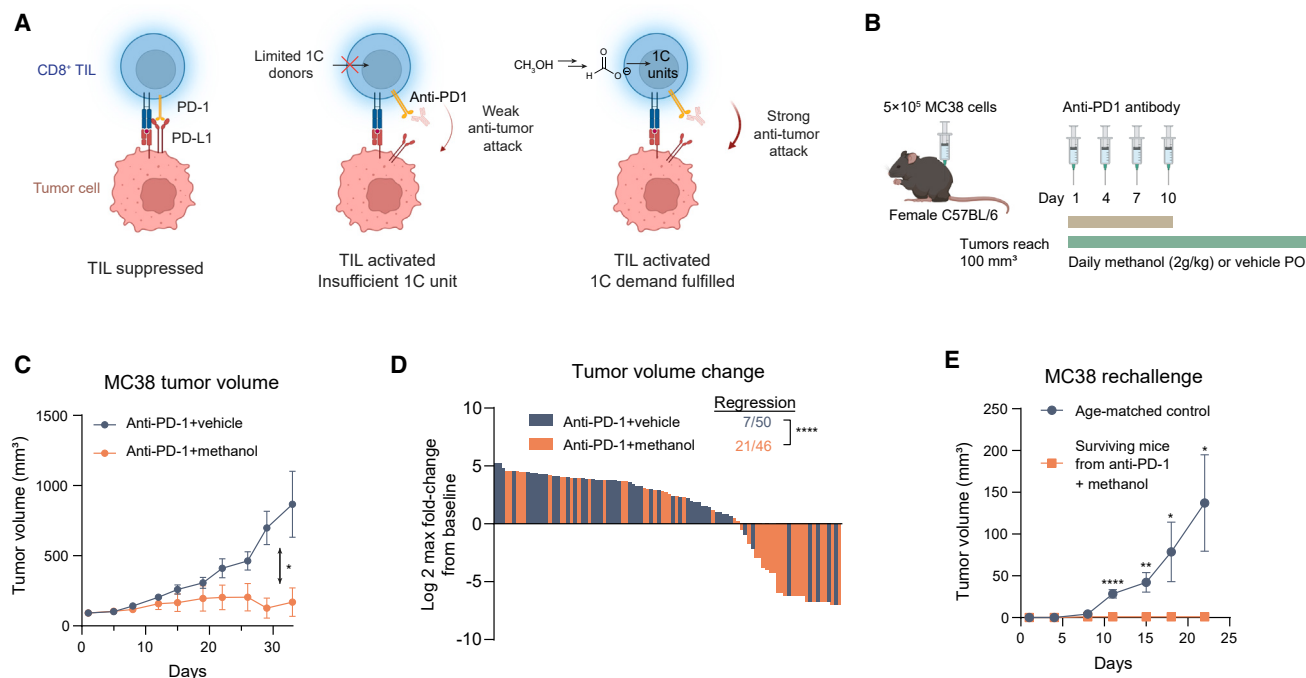


Figure 5. Methanol supplementation synergizes with PD-1 inhibition

(A) Model for methanol supplementation boosting PD-1 inhibition.

(B) Experimental design. Vehicle = 0.9% sodium chloride in water.

(C) MC38 tumor growth with anti-PD-1 ± methanol ($n = 10$). p value was determined by mixed ANOVA with repeated measures.

(D) Waterfall plot showing the maximal change in tumor volume compared to baseline (day 1) for each mouse, pooling data from four independent experiments (Figures S5B–S5E) with anti-PD-1 ± methanol. n is indicated on the plot. p value was determined by Pearson's chi-square test.

(E) Tumor growth after MC38 rechallenge in surviving mice from anti-PD-1 + methanol treatment group ($n = 6$) and age-matched controls ($n = 15$). p value was determined by Welch's t test for each time point. Mean ± SEM. n indicates the number of female mice. * $p < 0.05$; ** $p < 0.01$; *** $p < 0.001$; **** $p < 0.0001$. See also Figure S5.

anti-PD-1, methanol had no impact on tumor growth (Figure S5A). In combination with checkpoint blockade, however, methanol augmented tumor growth suppression (Figure 5C). This favorable interaction was strong in some experiments and not others, consistent with inherent variability of MC38 immunotherapy response (Figures S5B–S5E). Importantly, integrating data from four independent replicates, each with at least 10 mice per treatment group, the combination of methanol and anti-PD-1 markedly increased the frequency of durable regressions (Figure 5D). Consistent with the mechanism being via formate generation, supplementation of drinking water with formate showed a trend toward beneficial interaction with anti-PD-1 (Figures S5F and S5G), with formate drinking water recently reported to show synergy with checkpoint blockade in another murine cancer model (B16-OVA).⁴⁵ Consistent with *de novo* purine synthesis contributing more than salvage in TILs, we did not observe benefits from oral inosine (Figures S5H–S5J). This agrees with previous findings in the same tumor model.⁴⁶ While prior literature showed benefits from inosine supplementation in a different model,³⁴ these did not include durable regressions, the desired clinical outcome of immunotherapy. Regressions induced by anti-PD-1 + methanol were associated with persistent antitumor immunity, as reimplantation of fresh MC38 cancer cells resulted in tumor rejection in all mice that responded durably to their initial tumors (Figures 5E and S5K).

Thus, 1C unit supplementation via methanol as a formate pro-drug augments the activity of anti-PD-1 immunotherapy, increasing durable regressions.

Deuterium kinetic isotope effect can be used to control formate production rates

The primary safety risk of methanol ingestion is toxic formate buildup. This occurs when formate production by methanol oxidation outpaces formate clearance. In rodents, the balance of these reactions favors clearance of formate, rendering large doses of methanol safe, but mammals have lower formate clearance capacity.⁴⁴ We hypothesized that deuteration would slow methanol oxidation to formate, providing extended formate exposure at lower (safer) levels. In mice treated with [D₄]methanol, labeled plasma formate peaked around 100 μM, one-third the level of those treated with undeuterated [¹³C]methanol, and declined more gradually (Figure 6A). Notably, at a lower [¹³C] methanol dose that achieved an equivalent peak formate concentration, the duration of formate elevation was markedly shorter (Figure 6A). Similar patterns were also observed in cynomolgus monkeys (Figures 6B and 6C): deuteration doubled the half-life of methanol (Figure 6B), with 400 mg/kg steadily elevating plasma formate to 100 μM for 16 h (Figure 6C). Clearance of formate itself was not affected by deuteration (Figure S6A).

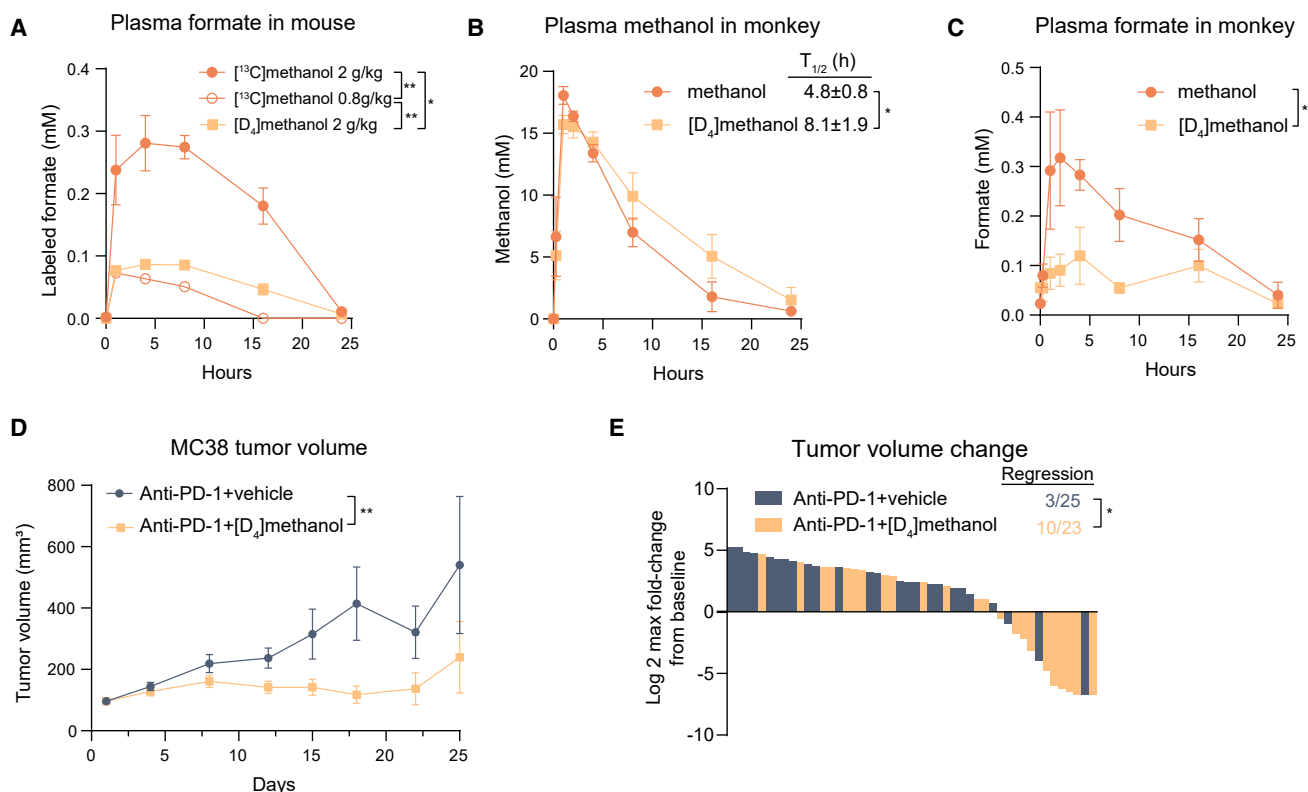


Figure 6. Deuterated methanol is a slow-release formate prodrug that augments immunotherapy

(A) Plasma $[^{13}\text{C}]$ or $[\text{D}]$ formate concentration over time after oral gavage of $[^{13}\text{C}]$ or $[\text{D}_4]$ methanol at 2 g/kg or 0.8 g/kg in mice ($n = 5$ males for $[^{13}\text{C}]$ at 2 g/kg, $n = 3$ males for others). p value was determined by mixed ANOVA with repeated measures.

(B) Plasma methanol and (C) formate concentration over time after oral gavage of methanol or $[\text{D}_4]$ methanol at 400 mg/kg in monkeys ($n = 3$ males). Half-life was fitted with an exponential decay model from 4 to 24 h. p value was determined by two-tailed Student's t test.

(D) MC38 tumor growth with anti-PD-1 \pm 2 g/kg $[\text{D}_4]$ methanol ($n = 15$ females for vehicle, $n = 13$ females for $[\text{D}_4]$ methanol). p value was determined by mixed ANOVA with repeated measures.

(E) Waterfall plot showing the maximal change in tumor volume compared to baseline (day 1) for each mouse, pooling data from 2 independent experiments (Figures S6B and S6C) with anti-PD-1 \pm methanol. n is indicated on the plot. p value was determined by Pearson chi-square test. Mean \pm SD in (B and C). Mean \pm SEM in (A) and (D). n indicates the number of animals. * $p < 0.05$; ** $p < 0.01$; *** $p < 0.001$; **** $p < 0.0001$. See also Figure S6.

We next examined whether $[\text{D}_4]$ methanol, like regular methanol, augments the activity of checkpoint blockade. Mice bearing MC38 tumors were treated with anti-PD-1 antibody, with and without daily gavage of $[\text{D}_4]$ methanol (2 g/kg). Despite subtler elevation of circulating formate (Figure 6A), tumor suppression was equally strong (Figure 6D), with the fraction of durable tumor regressions tripled across two independent experiments (Figures 6E and S6B–S6C), mirroring the result with regular methanol at the same dose (Figure 5D). Thus, deuterated methanol is a slow-release formate prodrug with the capacity to enhance immunotherapy.

DISCUSSION

Both cancer and activated immune cells reprogram metabolism to support their biosynthetic demands. One consistently upregulated pathway is 1C metabolism.^{19,47} Its enzymes support both tumor and T cell expansion²³ and T cell differentiation into effector subsets.²⁴ A major function of 1C metabolism is to support *de novo* purine synthesis. Here, using stable isotope tracing,

we show high activity of *de novo* purine synthesis in tumor-infiltrating T cells compared to CD8^+ T cells from spleen or tumor-draining lymph node. The 1C unit supply supporting such synthesis is a potential metabolic immune checkpoint, and we show that supplementing 1C units systemically synergizes with PD-1 inhibition.

On the flux level, our study provides *in vivo* evidence of CD8^+ T cells' dependence on *de novo* purine synthesis following activation and tumor infiltration. This result is consistent with a recent report that found increased TIL proliferation with formate supplementation and anti-PD-1, via a transitory exhausted CX3CR1^+ CD8^+ population.⁴⁵ Interestingly, this effect was specific to cancer-specific but not “bystander” TILs.⁴⁵ Given methanol's role as a formate prodrug, we expect similar immunological changes with combined methanol and anti-PD-1. However, future study is required to further examine nucleotide metabolism across various subpopulations of CD8^+ TILs and the immunological effect of methanol.

The benefits of 1C supplementation for cancer immunotherapy stand in contrast to the importance of 1C enzyme

inhibitors (antifolates) in cancer treatment. In current clinical oncology practice, the most important antifolate is pemetrexed, which preferentially targets thymidine synthesis. In contrast, methotrexate preferentially targets purine synthesis, and is now more commonly used as an immunosuppressant than cancer treatment. Indeed, low dose methotrexate to treat rheumatoid arthritis was shown to increase the risk of squamous cell carcinoma, likely due to immune suppression.⁴⁸ Thus, rather than considering the 1C pathway as a single entity, it is important to focus on specific enzymes, metabolites, and downstream products, with thymidine particularly important for cancer cells, and purines particularly important for immune cells.

To achieve 1C supplementation, we employed methanol as a formate prodrug. Methanol is converted by the sequential action of ADH and aldehyde dehydrogenase to formate, which is assimilated in the cytosol by the enzyme MTHFD1 to make 10-formyl-THF, a key purine biosynthetic input. Such supplementation did not just slow tumor growth under PD-1 inhibition, but resulted in durable tumor regressions in many mice, as did formate in the drinking water in a different tumor model in a recent report.⁴⁵ This differs from most metabolic strategies combined with anti-PD-1 to date, which tend to slow tumor growth but not result in durable regressions, e.g., supplementation of inosine,³⁴ methionine,¹² and arginine.⁴⁹ Instead, the preclinical results are more similar to, although somewhat less strong than, combination checkpoint therapies such as PD-1 and CTLA-4,^{50,51} which are clinically effective.^{52,53}

From a safety perspective, methanol is well known for its toxic effects on the visual system, causing blindness when consumed erroneously instead of ethanol. These toxic effects are not caused by methanol directly, but by formate, when it accumulates in excess of 5 mM.⁴³ At such high concentrations, formate results in metabolic acidosis and respiratory chain impairment, damaging the retina. The immunotherapy-enhancing formate concentrations achieved here are up to 50× lower, and can be maintained steadily at this level in monkeys using [D₄]methanol.

Interestingly, in human cancer patients, formate is among the most severely depleted circulating metabolites.⁵⁴ Moreover, folates, which are required for formate assimilation, are of lower abundance in humans than in mice.⁵⁵ Thus, it is tempting to speculate that 1C insufficiency is a yet bigger barrier to immunotherapy efficacy in the clinic than it is in mouse models. Clinical studies of 1C supplementation are merited to address this possibility.

Limitations of the study

The present research examines purine sources and 1C supplementation with methanol in a single immunocompetent murine tumor model, MC38. As is common in immunotherapy studies, efficacy varied across individual animals and experiments. Further work is required to understand the sources of this heterogeneity (e.g., microbiome and antigenicity of MC38 cells), as well as generality across additional murine tumor models.

Related recent research showed similar immunotherapy augmentation using direct formate supplementation in the B16-OVA tumor model.⁴⁵ The ¹³C-tracing data presented herein establish flux from methanol to circulating formate and T cell purine 1C units. Whether methanol may impact anti-tumor immunity via additional mechanisms beyond serving as a 1C donor

merits examination. Moreover, in addition to feeding T cells, formate might impact other cell types, e.g., myeloid cells, other innate immune cells, or tumor cells.

A final limitation regards safety. The beneficial effects of 1C supplementation were achieved here at formate levels below 0.5 mM, which appear to be safe based on substantial animal and human literature.^{43,56,57} Nevertheless, due to quantitative differences in methanol and formate metabolism between mice and primates, high-dose methanol can lead to toxic formate accumulation in humans. The data presented herein support methanol deuteration as a means of mitigating this risk, but additional pharmacokinetic and safety studies are required prior to human testing.

SIGNIFICANCE

Checkpoint blockade is now a mainstay of cancer therapy. Durable tumor control, however, is achieved in only a minority of patients. We show that the efficacy of anti-PD-1 blockade can be enhanced by metabolic supplementation with 1C donors. Such donors support nucleotide synthesis in tumor-infiltrating T cells and merit future clinical evaluation.

STAR★METHODS

Detailed methods are provided in the online version of this paper and include the following:

- KEY RESOURCES TABLE
- RESOURCE AVAILABILITY
 - Lead contact
 - Materials availability
 - Data and code availability
- EXPERIMENTAL MODEL AND STUDY PARTICIPANT DETAILS
 - Mouse
 - Monkey
 - Cell lines
 - Isolation, culture, and stimulation of mouse naive CD8⁺ T cells
- METHODS DETAILS
 - Mouse blood sampling
 - Measurement of circulatory turnover flux for nucleosides
 - Isotope tracing in cultured mouse CD8⁺ T cells
 - Mouse infusion
 - Formate and methanol dosing in monkeys
 - Magnetic activated cell sorting and metabolite extraction
 - Flow cytometry analysis
 - Tissue metabolite extraction
 - Formate derivatization
 - LC-MS method
 - GC-MS method
 - Formate measurement by ion chromatography
 - PD-1 efficacy with nutrient supplementation
 - Data analysis
- QUANTIFICATION AND STATISTICAL ANALYSIS

SUPPLEMENTAL INFORMATION

Supplemental information can be found online at <https://doi.org/10.1016/j.chembiol.2024.04.007>.

ACKNOWLEDGMENTS

J.D.R. was supported by Ludwig Cancer Research, R01CA163591 from the National Cancer Institute, DP1DK113643 from the National Institute of

Diabetes, Digestion and Kidney Disease, and SU2CAACR-DT-20-16 from Stand Up to Cancer. X.Xu and Z.C. were supported by the Edward C. Taylor Third Year Fellowship in Chemistry. C.R.B. was supported by the Damon Runyon Postdoctoral Fellowship. We thank John Eng at the Mass Spectrometry Core Facility for assistance with GC-MS. We also thank Christina DeCoste and Gabriel Palmieri at the Flow Cytometry Resource Facility. The Flow Cytometry Resource Facility was supported by NIH S10 award 1 S10OD028592-01A1. We thank Wenyun Lu, Yihui Shen, Tara TeSlaa, Won Dong Lee, and all other Rabinowitz lab members for insights and discussion.

AUTHOR CONTRIBUTIONS

J.D.R. and K.O. conceived the study. X.Xu and Z.C. came up with the general experimental strategy for *in vivo* tracing and performed most experiments. K.O. came up with the strategy for supplementing formate via methanol, designed and oversaw all PD-1 efficacy studies. Z.C. and C.R.B. optimized the cell isolation protocol. X.Xing wrote optCorr for natural isotope abundance correction. J.D.R., X.Xu, and Z.C. wrote the paper with inputs from all authors.

DECLARATION OF INTERESTS

J.D.R. is a paid adviser and/or stockholder in Colorado Research Partners, L.E.A.F. Pharmaceuticals, Faeth Therapeutics, and Empress Therapeutics; a paid consultant of Pfizer; a founder and stockholder in Marea Therapeutics; a founder, director, and stockholder of Farber Partners, Raze Therapeutics, and Sofro Pharmaceuticals. J.D.R. and K.O. are inventors of patent applications related to metabolic supplements that enhance immunotherapy.

Received: November 2, 2023

Revised: March 29, 2024

Accepted: April 17, 2024

Published: May 16, 2024

REFERENCES

- Vander Heiden, M.G., Cantley, L.C., and Thompson, C.B. (2009). Understanding the Warburg Effect: The Metabolic Requirements of Cell Proliferation. *Science* 324, 1029–1033. <https://doi.org/10.1126/science.1160809>.
- Pavlova, N.N., and Thompson, C.B. (2016). The Emerging Hallmarks of Cancer Metabolism. *Cell Metab.* 23, 27–47. <https://doi.org/10.1016/j.cmet.2015.12.006>.
- Overholtzer, M., Mailloux, A.A., Mouneimne, G., Normand, G., Schnitt, S.J., King, R.W., Cibas, E.S., and Brugge, J.S. (2007). A Nonapoptotic Cell Death Process, Entosis, that Occurs by Cell-in-Cell Invasion. *Cell* 131, 966–979. <https://doi.org/10.1016/j.cell.2007.10.040>.
- Finicle, B.T., Jayashankar, V., and Edinger, A.L. (2018). Nutrient scavenging in cancer. *Nat. Rev. Cancer* 18, 619–633. <https://doi.org/10.1038/s41568-018-0048-x>.
- Commisso, C., Davidson, S.M., Soydaner-Azeloglu, R.G., Parker, S.J., Kamphorst, J.J., Hackett, S., Grabocka, E., Nofal, M., Drebin, J.A., Thompson, C.B., et al. (2013). Macropinocytosis of protein is an amino acid supply route in Ras-transformed cells. *Nature* 497, 633–637. <https://doi.org/10.1038/nature12138>.
- Davidson, S.M., Jonas, O., Keibler, M.A., Hou, H.W., Luengo, A., Mayers, J.R., Wyckoff, J., Del Rosario, A.M., Whitman, M., Chin, C.R., et al. (2017). Direct evidence for cancer-cell-autonomous extracellular protein catabolism in pancreatic tumors. *Nat. Med.* 23, 235–241. <https://doi.org/10.1038/nm.4256>.
- DePeaux, K., and Delgoffe, G.M. (2021). Metabolic barriers to cancer immunotherapy. *Nat. Rev. Immunol.* 21, 785–797. <https://doi.org/10.1038/s41577-021-00541-y>.
- Chang, C.-H., Qiu, J., O'Sullivan, D., Buck, M.D., Noguchi, T., Curtis, J.D., Chen, Q., Gindin, M., Gubin, M.M., van der Windt, G.J.W., et al. (2015). Metabolic Competition in the Tumor Microenvironment Is a Driver of Cancer Progression. *Cell* 162, 1229–1241. <https://doi.org/10.1016/j.cell.2015.08.016>.
- Ho, P.-C., Bihuniak, J.D., Macintyre, A.N., Staron, M., Liu, X., Amezcua, R., Tsui, Y.-C., Cui, G., Micevic, G., Perales, J.C., et al. (2015). Phosphoenolpyruvate Is a Metabolic Checkpoint of Anti-tumor T Cell Responses. *Cell* 162, 1217–1228. <https://doi.org/10.1016/j.cell.2015.08.012>.
- Reinfeld, B.I., Madden, M.Z., Wolf, M.M., Chytil, A., Bader, J.E., Patterson, A.R., Sugiura, A., Cohen, A.S., Ali, A., Do, B.T., et al. (2021). Cell-programmed nutrient partitioning in the tumour microenvironment. *Nature* 593, 282–288. <https://doi.org/10.1038/s41586-021-03442-1>.
- Geiger, R., Rieckmann, J.C., Wolf, T., Basso, C., Feng, Y., Fuhrer, T., Kogadeeva, M., Picotti, P., Meissner, F., Mann, M., et al. (2016). L-Arginine Modulates T Cell Metabolism and Enhances Survival and Anti-tumor Activity. *Cell* 167, 829–842.e13. <https://doi.org/10.1016/j.cell.2016.09.031>.
- Bian, Y., Li, W., Kremer, D.M., Sajjakulnukit, P., Li, S., Crespo, J., Nwosu, Z.C., Zhang, L., Czerwonka, A., Pawlowska, A., et al. (2020). Cancer SLC43A2 alters T cell methionine metabolism and histone methylation. *Nature* 585, 277–282. <https://doi.org/10.1038/s41586-020-2682-1>.
- Scharping, N.E., Menk, A.V., Whetstone, R.D., Zeng, X., and Delgoffe, G.M. (2017). Efficacy of PD-1 Blockade Is Potentiated by Metformin-Induced Reduction of Tumor Hypoxia. *Cancer Immunol. Res.* 5, 9–16. <https://doi.org/10.1158/2326-6066.CIR-16-0103>.
- Najjar, Y.G., Menk, A.V., Sander, C., Rao, U., Karunamurthy, A., Bhatia, R., Zhai, S., Kirkwood, J.M., and Delgoffe, G.M. (2019). Tumor cell oxidative metabolism as a barrier to PD-1 blockade immunotherapy in melanoma. *JCI Insight* 4, e124989. <https://doi.org/10.1172/jci.insight.124989>.
- Quinn, W.J., Jiao, J., TeSlaa, T., Stadanlick, J., Wang, Z., Wang, L., Akimova, T., Angelin, A., Schäfer, P.M., Cully, M.D., et al. (2020). Lactate Limits T Cell Proliferation via the NAD(H) Redox State. *Cell Rep.* 33, 108500. <https://doi.org/10.1016/j.celrep.2020.108500>.
- Opitz, C.A., Litzenburger, U.M., Sahm, F., Ott, M., Tritschler, I., Trump, S., Schumacher, T., Jestaedt, L., Schrenk, D., Weller, M., et al. (2011). An endogenous tumour-promoting ligand of the human aryl hydrocarbon receptor. *Nature* 478, 197–203. <https://doi.org/10.1038/nature10491>.
- Long, G.V., Dummer, R., Hamid, O., Gajewski, T.F., Cagle, C., Dalle, S., Arance, A., Carlino, M.S., Grob, J.-J., Kim, T.M., et al. (2019). Epcadostat plus pembrolizumab versus placebo plus pembrolizumab in patients with unresectable or metastatic melanoma (ECHO-301/KEYNOTE-252): a phase 3, randomised, double-blind study. *Lancet Oncol.* 20, 1083–1097. [https://doi.org/10.1016/S1470-2045\(19\)30274-8](https://doi.org/10.1016/S1470-2045(19)30274-8).
- Farber, S., Diamond, L.K., Mercer, R.D., Sylvester, R.F., and Wolff, J.A. (1948). Temporary Remissions in Acute Leukemia in Children Produced by Folic Acid Antagonist, 4-Aminopteroyl-Glutamic Acid (Aminopterin). *N. Engl. J. Med.* 238, 787–793. <https://doi.org/10.1056/NEJM194806032382301>.
- Ducker, G.S., and Rabinowitz, J.D. (2017). One-Carbon Metabolism in Health and Disease. *Cell Metab.* 25, 27–42. <https://doi.org/10.1016/j.cmet.2016.08.009>.
- Kamatani, N., Jinnah, H.A., Hennekam, R.C.M., and van Kuilenburg, A.B.P. (2021). Purine and Pyrimidine Metabolism. In *Emery and Rimoin's Principles and Practice of Medical Genetics and Genomics* (Elsevier), pp. 183–234. <https://doi.org/10.1016/B978-0-12-812535-9.00006-6>.
- Asselin, B.L., Devidas, M., Wang, C., Pullen, J., Borowitz, M.J., Hutchison, R., Lipschultz, S.E., and Camitta, B.M. (2011). Effectiveness of high-dose methotrexate in T-cell lymphoblastic leukemia and advanced-stage lymphoblastic lymphoma: a randomized study by the Children's Oncology Group (POG 9404). *Blood* 118, 874–883. <https://doi.org/10.1182/blood-2010-06-292615>.
- Brown, P.M., Pratt, A.G., and Isaacs, J.D. (2016). Mechanism of action of methotrexate in rheumatoid arthritis, and the search for biomarkers. *Nat. Rev. Rheumatol.* 12, 731–742. <https://doi.org/10.1038/nrrheum.2016.175>.
- Ma, E.H., Bantug, G., Griss, T., Condotta, S., Johnson, R.M., Samborska, B., Mainolfi, N., Suri, V., Guak, H., Balmer, M.L., et al. (2017). Serine Is an Essential Metabolite for Effector T Cell Expansion. *Cell Metab.* 25, 345–357. <https://doi.org/10.1016/j.cmet.2016.12.011>.

24. Sugiura, A., Andrejeva, G., Voss, K., Heintzman, D.R., Xu, X., Madden, M.Z., Ye, X., Beier, K.L., Chowdhury, N.U., Wolf, M.M., et al. (2022). MTHFD2 is a metabolic checkpoint controlling effector and regulatory T cell fate and function. *Immunity* 55, 65–81.e9. <https://doi.org/10.1016/j.immuni.2021.10.011>.
25. Belk, J.A., Yao, W., Ly, N., Freitas, K.A., Chen, Y.-T., Shi, Q., Valencia, A.M., Shifrut, E., Kale, N., Yost, K.E., et al. (2022). Genome-wide CRISPR screens of T cell exhaustion identify chromatin remodeling factors that limit T cell persistence. *Cancer Cell* 40, 768–786.e7. <https://doi.org/10.1016/j.ccell.2022.06.001>.
26. Traut, T.W. (1994). Physiological concentrations of purines and pyrimidines. *Mol. Cell. Biochem.* 140, 1–22. <https://doi.org/10.1007/BF00928361>.
27. Jabs, C.M., Sigurdsson, G.H., and Neglen, P. (1998). Plasma levels of high-energy compounds compared with severity of illness in critically ill patients in the intensive care unit. *Surgery* 124, 65–72.
28. Niwa, T., Takeda, N., and Yoshizumi, H. (1998). RNA metabolism in uremic patients: Accumulation of modified ribonucleosides in uremic serum. *Kidney Int.* 53, 1801–1806. <https://doi.org/10.1046/j.1523-1755.1998.00944.x>.
29. Nyhan, W.L. (1997). The recognition of Lesch-Nyhan syndrome as an inborn error of purine metabolism. *J. Inher. Metab. Dis.* 20, 171–178. <https://doi.org/10.1023/A:1005348504512>.
30. Flinn, A.M., and Gennery, A.R. (2018). Adenosine deaminase deficiency: a review. *Orphanet J. Rare Dis.* 13, 65. <https://doi.org/10.1186/s13023-018-0807-5>.
31. Markert, M.L. (1991). Purine nucleoside phosphorylase deficiency. *Immunodef. Rev.* 3, 45–81.
32. Beran, J., Šalapová, E., and Špajdel, M.; Isoprinosine Study EWO ISO-2014/1 Team (2016). Inosine pranobex is safe and effective for the treatment of subjects with confirmed acute respiratory viral infections: analysis and subgroup analysis from a Phase 4, randomised, placebo-controlled, double-blind study. *BMC Infect. Dis.* 16, 648. <https://doi.org/10.1186/s12879-016-1965-5>.
33. Sliva, J., Pantartzis, C.N., and Votava, M. (2019). Inosine Pranobex: A Key Player in the Game Against a Wide Range of Viral Infections and Non-Infectious Diseases. *Adv. Ther.* 36, 1878–1905. <https://doi.org/10.1007/s12325-019-00995-6>.
34. Mager, L.F., Burkhard, R., Pett, N., Cooke, N.C.A., Brown, K., Ramay, H., Paik, S., Stagg, J., Groves, R.A., Gallo, M., et al. (2020). Microbiome-derived inosine modulates response to checkpoint inhibitor immunotherapy. *Science* 369, 1481–1489. <https://doi.org/10.1126/science.abc3421>.
35. Burgos-Barragan, G., Wit, N., Meiser, J., Dingler, F.A., Pietzke, M., Mulderrig, L., Pontel, L.B., Rosado, I.V., Brewer, T.F., Cordell, R.L., et al. (2017). Mammals divert endogenous genotoxic formaldehyde into one-carbon metabolism. *Nature* 548, 549–554. <https://doi.org/10.1038/nature23481>.
36. Meiser, J., Tumanov, S., Maddocks, O., Labuschagne, C.F., Athineos, D., Van Den Broek, N., Mackay, G.M., Gottlieb, E., Blyth, K., Vousden, K., et al. (2016). Serine one-carbon catabolism with formate overflow. *Sci. Adv.* 2, e1601273. <https://doi.org/10.1126/sciadv.1601273>.
37. Aran, D., Hu, Z., and Butte, A.J. (2017). xCell: digitally portraying the tissue cellular heterogeneity landscape. *Genome Biol.* 18, 220. <https://doi.org/10.1186/s13059-017-1349-1>.
38. Raskov, H., Orhan, A., Christensen, J.P., and Gögenur, I. (2021). Cytotoxic CD8+ T cells in cancer and cancer immunotherapy. *Br. J. Cancer* 124, 359–367. <https://doi.org/10.1038/s41416-020-01048-4>.
39. Ma, E.H., Verway, M.J., Johnson, R.M., Roy, D.G., Steadman, M., Hayes, S., Williams, K.S., Sheldon, R.D., Samborska, B., Kosinski, P.A., et al. (2019). Metabolic Profiling Using Stable Isotope Tracing Reveals Distinct Patterns of Glucose Utilization by Physiologically Activated CD8+ T Cells. *Immunity* 51, 856–870.e5. <https://doi.org/10.1016/j.immuni.2019.09.003>.
40. Sheldon, R.D., Ma, E.H., DeCamp, L.M., Williams, K.S., and Jones, R.G. (2021). Interrogating in vivo T-cell metabolism in mice using stable isotope labeling metabolomics and rapid cell sorting. *Nat. Protoc.* 16, 4494–4521. <https://doi.org/10.1038/s41596-021-00586-2>.
41. Kilgour, M.K., MacPherson, S., Zacharias, L.G., LeBlanc, J., Babinszky, S., Kowalchuk, G., Parks, S., Sheldon, R.D., Jones, R.G., DeBerardinis, R.J., et al. (2022). Principles of reproducible metabolite profiling of enriched lymphocytes in tumors and ascites from human ovarian cancer. *Nat. Protoc.* 17, 2668–2698. <https://doi.org/10.1038/s41596-022-00729-z>.
42. Hui, S., Ghergurovich, J.M., Morscher, R.J., Jang, C., Teng, X., Lu, W., Esparza, L.A., Reya, T., Le, Z., Yanxiang Guo, J., et al. (2017). Glucose feeds the TCA cycle via circulating lactate. *Nature* 551, 115–118. <https://doi.org/10.1038/nature24057>.
43. Zakharov, S., Kurcova, I., Navratil, T., Salek, T., Komarc, M., and Pelclova, D. (2015). Is the Measurement of Serum Formate Concentration Useful in the Diagnostics of Acute Methanol Poisoning? A Prospective Study of 38 Patients. *Basic Clin. Pharmacol. Toxicol.* 116, 445–451. <https://doi.org/10.1111/bcpt.12338>.
44. Jacobsen, D., and McMartin, K.E. (1986). Methanol and Ethylene Glycol Poisonings. *Med. Toxicol.* 1, 309–334. <https://doi.org/10.1007/BF03259846>.
45. Rowe, J.H., Elia, I., Shahid, O., Gaudiano, E.F., Sifnugel, N.E., Johnson, S., Reynolds, A.G., Fung, M.E., Joshi, S., LaFleur, M.W., et al. (2023). Formate Supplementation Enhances Antitumor CD8+ T-cell Fitness and Efficacy of PD-1 Blockade. *Cancer Discov.* 13, 2566–2583. <https://doi.org/10.1158/2159-8290.CD-22-1301>.
46. Wang, T., Gnanaprakasam, J.N.R., Chen, X., Kang, S., Xu, X., Sun, H., Liu, L., Rodgers, H., Miller, E., Cassel, T.A., et al. (2020). Inosine is an alternative carbon source for CD8+ T-cell function under glucose restriction. *Nat. Metab.* 2, 635–647. <https://doi.org/10.1038/s42255-020-0219-4>.
47. Tan, H., Yang, K., Li, Y., Shaw, T.I., Wang, Y., Blanco, D.B., Wang, X., Cho, J.-H., Wang, H., Rankin, S., et al. (2017). Integrative Proteomics and Phosphoproteomics Profiling Reveals Dynamic Signaling Networks and Bioenergetics Pathways Underlying T Cell Activation. *Immunity* 46, 488–503. <https://doi.org/10.1016/j.immuni.2017.02.010>.
48. Vanni, K.M.M., Berliner, N., Paynter, N.P., Glynn, R.J., MacFadyen, J., Colls, J., Lu, F., Xu, C., Ridker, P.M., and Solomon, D.H. (2020). Adverse Effects of Low-Dose Methotrexate in a Randomized Double-Blind Placebo-Controlled Trial: Adjudicated Hematologic and Skin Cancer Outcomes in the Cardiovascular Inflammation Reduction Trial. *ACR Open Rheumatol.* 2, 697–704. <https://doi.org/10.1002/acr2.11187>.
49. He, X., Lin, H., Yuan, L., and Li, B. (2017). Combination therapy with L-arginine and α -PD-L1 antibody boosts immune response against osteosarcoma in immunocompetent mice. *Cancer Biol. Ther.* 18, 94–100. <https://doi.org/10.1080/15384047.2016.1276136>.
50. Duraiswamy, J., Kaluza, K.M., Freeman, G.J., and Coukos, G. (2013). Dual Blockade of PD-1 and CTLA-4 Combined with Tumor Vaccine Effectively Restores T-Cell Rejection Function in Tumors. *Cancer Res.* 73, 3591–3603. <https://doi.org/10.1158/0008-5472.CAN-12-4100>.
51. Curran, M.A., Montalvo, W., Yagita, H., and Allison, J.P. (2010). PD-1 and CTLA-4 combination blockade expands infiltrating T cells and reduces regulatory T and myeloid cells within B16 melanoma tumors. *Proc. Natl. Acad. Sci.* 107, 4275–4280. <https://doi.org/10.1073/pnas.0915174107>.
52. Hodi, F.S., Chesney, J., Pavlick, A.C., Robert, C., Grossmann, K.F., McDermott, D.F., Linette, G.P., Meyer, N., Giguere, J.K., Agarwala, S.S., et al. (2016). Combined nivolumab and ipilimumab versus ipilimumab alone in patients with advanced melanoma: 2-year overall survival outcomes in a multicentre, randomised, controlled, phase 2 trial. *Lancet Oncol.* 17, 1558–1568. [https://doi.org/10.1016/S1470-2045\(16\)30366-7](https://doi.org/10.1016/S1470-2045(16)30366-7).
53. Hellmann, M.D., Ciuleanu, T.-E., Pluzanski, A., Lee, J.S., Otterson, G.A., Audigier-Valette, C., Minenza, E., Linardou, H., Burgers, S., Salman, P., et al. (2018). Nivolumab plus ipilimumab in Lung Cancer with a High Tumor Mutational Burden. *N. Engl. J. Med.* 378, 2093–2104. <https://doi.org/10.1056/NEJMoa1801946>.

54. Pietzke, M., Arroyo, S.F., Sumpton, D., Mackay, G.M., Martin-Castillo, B., Camps, J., Joven, J., Menendez, J.A., Vazquez, A., METTEN study group, et al. (2019). Stratification of cancer and diabetes based on circulating levels of formate and glucose. *Cancer Metab.* 7, 3. <https://doi.org/10.1186/s40170-019-0195-x>.
55. Ghergurovich, J.M., Xu, X., Wang, J.Z., Yang, L., Ryseck, R.-P., Wang, L., and Rabinowitz, J.D. (2021). Methionine synthase supports tumour tetrahydrofolate pools. *Nat. Metab.* 3, 1512–1520. <https://doi.org/10.1038/s42255-021-00465-w>.
56. Røe, O., and Enoksson, P. (1982). Species Differences in Methanol Poisoning. *CRC Crit. Rev. Toxicol.* 10, 275–286. <https://doi.org/10.3109/10408448209003368>.
57. Hovda, K.E., Urdal, P., and Jacobsen, D. (2005). Increased Serum Formate in the Diagnosis of Methanol Poisoning. *J. Anal. Toxicol.* 29, 586–588. <https://doi.org/10.1093/jat/29.6.586>.
58. Xing, X. (2024). xxing9703/optCorr_script: v1.0.1. Version v1.0.1 (Zenodo). <https://doi.org/10.5281/zenodo.10976652>.
59. Ghergurovich, J.M., García-Cañaveras, J.C., Wang, J., Schmidt, E., Zhang, Z., TeSlaa, T., Patel, H., Chen, L., Britt, E.C., Piqueras-Nebot, M., et al. (2020). A small molecule G6PD inhibitor reveals immune dependence on pentose phosphate pathway. *Nat. Chem. Biol.* 16, 731–739. <https://doi.org/10.1038/s41589-020-0533-x>.
60. Shen, Y., Dinh, H.V., Cruz, E.R., Chen, Z., Bartman, C.R., Xiao, T., Call, C.M., Ryseck, R.-P., Pratas, J., Weilandt, D., et al. (2024). Mitochondrial ATP generation is more proteome efficient than glycolysis. *Nat. Chem. Biol.* 1–10. <https://doi.org/10.1038/s41589-024-01571-y>.
61. Rabinowitz, J.D., and Kimball, E. (2007). Acidic Acetonitrile for Cellular Metabolome Extraction from *Escherichia coli*. *Anal. Chem.* 79, 6167–6173. <https://doi.org/10.1021/ac070470c>.
62. Zeng, X., Xing, X., Gupta, M., Keber, F.C., Lopez, J.G., Lee, Y.-C.J., Roichman, A., Wang, L., Neinast, M.D., Donia, M.S., et al. (2022). Gut bacterial nutrient preferences quantified in vivo. *Cell* 185, 3441–3456.e19. <https://doi.org/10.1016/j.cell.2022.07.020>.
63. Chambers, M.C., Maclean, B., Burke, R., Amodei, D., Ruderman, D.L., Neumann, S., Gatto, L., Fischer, B., Pratt, B., Egertson, J., et al. (2012). A cross-platform toolkit for mass spectrometry and proteomics. *Nat. Biotechnol.* 30, 918–920. <https://doi.org/10.1038/nbt.2377>.
64. Agrawal, S., Kumar, S., Sehgal, R., George, S., Gupta, R., Poddar, S., Jha, A., and Pathak, S. (2019). EI-MAVEN: A Fast, Robust, and User-Friendly Mass Spectrometry Data Processing Engine for Metabolomics. In *High-Throughput Metabolomics: Methods and Protocols*, A. D'Alessandro, ed. (Springer), pp. 301–321. https://doi.org/10.1007/978-1-4939-9236-2_19.
65. Su, X., Lu, W., and Rabinowitz, J.D. (2017). Metabolite Spectral Accuracy on Orbitraps. *Anal. Chem.* 89, 5940–5948. <https://doi.org/10.1021/acs.analchem.7b00396>.

STAR★METHODS

KEY RESOURCES TABLE

REAGENT or RESOURCE	SOURCE	IDENTIFIER
Antibodies		
Anti-mouse PD-1 (clone RMP1-14, low endotoxin)	ichorbio	CAT# ICH1132; RRID: AB_2921498
Rat IgG2a (clone 2A3)	BioXcell	CAT# BE0089; RRID: AB_1107769
Anti-mouse CD3 ϵ (clone 145-2C11)	BioXcell	CAT# BE0001-1; RRID: AB_2687679
Anti-mouse CD28 (clone 37.51)	BioXcell	CAT# BE0015-1; RRID: AB_1107624
Anti-mouse CD4 (clone RM4-5) APC-Cy7	BD Biosciences	CAT# 565650; RRID: AB_2739324
Anti-mouse CD4 (clone GK1.5) BUV805	BD Biosciences	CAT# 612900; RRID: AB_2739008
Anti-mouse CD8a (clone 53-6.7) Alexa Fluor 700	Biolegend	CAT#100730; RRID: AB_493703
Anti-mouse CD8b (clone YTS156.7.7) Alexa Fluor 488	Biolegend	CAT# 126628; RRID: AB_2800619
Anti-mouse CD45.2 (clone 104) eFluor 450	Thermo Fisher	CAT# 48-0454-82; RRID: AB_11042125
Anti-mouse CD45.2 (clone 104) APC-Cy7	Biolegend	CAT# 109824; RRID: AB_830789
Anti-mouse CD62L (clone MEL-14) PE-Cy7	BD Biosciences	CAT# 560516; RRID: AB_1645257
Anti-mouse CD69 (clone H1.2F3) PE-CF594	BD Biosciences	CAT# 562455; RRID: AB_11154217
Chemicals, peptides, and recombinant proteins		
DMEM medium	Corning	CAT# 10-017-CV
RPMI 1640 medium	Gibco	CAT# 11875-093
Fetal bovine serum	Sigma	CAT# F2442, lot#20C567
Fetal bovine serum, heat inactivated	Corning	CAT# 35-011-CV, lot#23623001
Dialyzed fetal bovine serum	Sigma	CAT# F0392, lot#20A360
DNase	Sigma-Aldrich	CAT# D5025
Collagenase	Sigma-Aldrich	CAT# C2674
RBC lysis buffer	Invitrogen	CAT# 00-4300-54
Mouse IL-7 recombinant protein	PeproTech	CAT# 217-17
Mouse IL-2 recombinant protein	PeproTech	CAT# 212-12
Propidium iodide ready flow reagent	Invitrogen	CAT# R37169
DAPI Solution	Thermo Scientific	CAT# 62248
[U- ¹⁵ N]inosine	Cambridge Isotope Laboratories	CAT# NLM-4264-PK
[U- ¹⁵ N]adenosine	Cambridge Isotope Laboratories	CAT# NLM-9750-SL
[U- ¹⁵ N]uridine	Cambridge Isotope Laboratories	CAT# NLM-812-PK
[U- ¹⁵ N]cytidine	Cambridge Isotope Laboratories	CAT# NLM-3797-PK
[U- ¹⁵ N]thymidine	Cambridge Isotope Laboratories	CAT# NLM-3901-PK
[U- ¹³ C]L-serine	Cambridge Isotope Laboratories	CAT# CLM-1574-H-PK
[amide- ¹⁵ N]L-glutamine	Cambridge Isotope Laboratories	CAT# NLM-557-PK
[¹³ C]sodium formate	Cambridge Isotope Laboratories	CAT# CLM-583-PK
[D ₄]methanol	Cambridge Isotope Laboratories	CAT# DLM-24-PK
Critical commercial assays		
CD8 (TIL) microBeads, mouse	Miltenyi Biotec	CAT# 130-116-478
Fixable aqua dead cell stain kit	Invitrogen	CAT# L34966
Naive CD8a ⁺ T cell isolation kit, mouse	Miltenyi Biotec	CAT# 130-096-543
RPMI 1640 medium w/o L-glutamine, L-serine	USBiological	CAT# R8999-15
Deposited data		
Metabolomics data sets related to Figures S1B, S1C, and S1D	This paper	MassIVE: MSV000094432
Experimental models: Cell lines		
MC38	Kerafast	CAT# ENH204-FP; RRID: CVCL_B288

(Continued on next page)

REAGENT or RESOURCE	SOURCE	IDENTIFIER
Continued		
Experimental models: Organisms/strains		
C57BL/6 mice	Charles River Laboratories	CAT# 027
Cynomolgus monkeys (<i>Macaca fascicularis</i>)	Hainan Jingang Biotech	N/A
Software and algorithms		
FCS Express 7.12	De Novo Software	https://denovosoftware.com/
MSCConvert	ProteoWizard	https://proteowizard.sourceforge.io
EI Maven 0.8.0	Elucidata	An archived record is available at https://github.com/ElucidataInc/EIMaven , or via https://doi.org/10.5281/zenodo.3362126
'accucor' natural abundance correction	Github	https://github.com/XiaoyangSu/AccuCor
'optCorr' natural abundance correction	This paper	https://github.com/xxing9703/optCorr_script , or via https://doi.org/10.5281/zenodo.10976652
GraphPad Prism 10	GraphPad Software	https://www.graphpad.com
Other		
PicoLab rodent diet 5053	LabDiet	CAT# 5053
NIH-31M auto chow	Ziegler Feed	CAT# NIH-31M
MidiMACS separators	Miltenyi Biotec	CAT# 130-042-303
LS columns	Miltenyi Biotec	CAT# 130-042-401
Catheter for mouse jugular vein	Instech	CAT# C20PU-MJV1301
Catheter for mouse carotid artery	Instech	CAT# C10PU-MCA1459
One-channel vascular access button	Instech	CAT# VABM1B/25
Two-channel vascular access button	Instech	CAT# VABM2B/25R25
LSR II flow cytometer	BD Biosciences	N/A
FACSymphony A3 flow cytometer	BD Biosciences	N/A
Q Exactive Plus quadrupole-orbitrap mass spectrometer	Thermo Scientific	CAT# IQLAAEGAAPFALGMBDK
Orbitrap Exploris 240 mass spectrometer	Thermo Scientific	CAT# BRE725535
Orbitrap Exploris 480 mass spectrometer	Thermo Scientific	CAT# BRE725539
7250 GC/Q-TOF	Agilent	CAT# G7250AA
XBridge BEH amide column	Waters	CAT# 186006724
Acquity UPLC BEH C18 column	Waters	CAT# 186002352
VF-WAXms fused silica GC column	Agilent	CAT# CP9222

RESOURCE AVAILABILITY

Lead contact

Further information and requests for resources and reagents should be directed to and will be fulfilled by the lead contact, Joshua D. Rabinowitz (joshr@princeton.edu).

Materials availability

This study did not generate new unique reagents.

Data and code availability

- Raw metabolomics data have been deposited at massive.ucsd.edu (MassIVE: MSV000094432) and are publicly available. All source data to generate figures are supplied as [Table S2](#).
- 'optCorr',⁵⁸ a natural isotope correction package for partially resolved MS peaks is available at https://github.com/xxing9703/optCorr_script. An archived record is available via <https://doi.org/10.5281/zenodo.10976651>.
- Any additional information required to reanalyze the data reported in this paper is available from the [lead contact](#) upon request.

EXPERIMENTAL MODEL AND STUDY PARTICIPANT DETAILS

Mouse

All mouse experiments were approved by the Institutional Animal Care and Use Committee at Princeton University and Charles River Laboratories. Experiments for testing anti-PD-1 efficacy were performed at Charles River Laboratories. All other mouse experiments were performed at Princeton University. C57BL/6 mice from Charles River Laboratories were used at the age of 9–15 weeks, with sex noted in figure legends. Mice were housed under a normal light cycle (7 AM to 7 PM), with water and food (PicoLab Rodent Diet 5053, LabDiet) provided *ad libitum*. Jugular vein and/or carotid artery catheterization was performed in house. With sterile technique, catheters (C20PU-MJV1301 or C10PU-MCA1459, Instech) were inserted into the right jugular vein and (for arterial sampling) the left carotid artery and connected to a vascular access button (one-channel VABM1B/25 or two-channel VABM2B/25R25, Instech) implanted subcutaneously on the back of the mouse. Mice were allowed to recover for at least 5 days after surgery. To maintain catheter patency, catheters were flushed weekly with heparin saline (10 IU/mL) and locked by a catheter locking solution (500 IU/mL heparin in 50% glycerol, SAI Infusion Technologies).

Monkey

Experiments involving cynomolgus monkeys (*Macaca fascicularis*) were approved by the Institutional Animal Care and Use Committee at WuXi AppTec Co. Male monkeys (purchased from Hainan Jingang Biotech) were used at the age of 31–44 months. Following arrival at WuXi, animals were assessed as to their general health by a member of the veterinary staff or other authorized personnel. Animals were acclimated for least 14 days (upon arrival at WuXi AppTec) before being placed on study. The room was controlled and monitored for relative humidity (40%–70%) and temperature (18°C–26°C) with no less than 10 air changes/hour. The room was on a 12-hour light/dark cycle. Animals were individually housed in stainless-steel mesh cages during in-life that was in accordance with the National Research Council "Guide for the Care and Use of Laboratory Animals". Animals were fed twice daily with approximately 120 grams of Certified Monkey Diet in total. In addition, animals received fruit daily as nutritional enrichment. For fasted animals, animals were fed the afternoon prior to the day of dosing and the remaining food was removed at night. Food was withheld until 4-hour post-dose unless specified in this protocol. Fasted animals were fed once on the day of dosing with the amount of approximately 120 g. Reverses osmosis water was available to all animals, *ad libitum*.

Cell lines

The MC38 cell line derived from female C57BL/6 mice was obtained from Kerastat (Boston, MA) and maintained at 37°C and 5% CO₂ in Dulbecco's Modified Eagle Medium (10-017-CV, Corning) supplemented with 10 vol% fetal bovine serum (F2442, Sigma). Cell line authentication data and pathogen testing results are available at: <https://www.kerastat.com/productgroup/665/mc-38-cell-line>. To initiate tumors for infusion studies, cells were trypsinized, washed once with phosphate buffered saline (PBS), resuspended in PBS and kept on ice. $0.5\text{--}1 \times 10^6$ cells were injected subcutaneously in 100 μL of PBS on the left flank of each mouse. Tumors were measured twice per week, with tumor size calculated by $0.5 \times \text{length} \times \text{width} \times \text{height}$. Tracing experiments were performed when tumors reached 150–450 mm³ (2–3 weeks after implantation).

Isolation, culture, and stimulation of mouse naive CD8⁺ T cells

Procedures were adapted from Ghergurovich et al.⁵⁹ and Shen et al.⁶⁰ To isolate naive CD8⁺ T cells, spleens from female mice at 8 weeks old were collected and pooled as single-cell suspensions by manual disruption and passage through 40- μm cell strainers into RPMI-1640 medium (11875-093, Gibco). After RBC lysis (00-4300-54, Invitrogen), naive CD8⁺ T cells were purified by magnetic bead separation using naive CD8a⁺ T cell Isolation Kit, mouse (130-096-543, Miltenyi Biotec Inc.) following vendor instructions.

Cells were cultured at 1×10^6 cells ml⁻¹ in complete RPMI medium (RPMI-1640 medium, 10% heat inactivated FBS (35-011-CV, Corning), 100 U ml⁻¹ penicillin, 100 μg ml⁻¹ streptomycin (15140-122, Gibco) and 55 μM 2-mercaptoethanol (21985-023, Gibco)). Naive T cells were either rested in complete RPMI medium with recombinant murine IL-7 (5 ng ml⁻¹; 217-17, Peprotech) or stimulated for 24 h with plate-bound anti-CD3 (10 μg ml⁻¹; BE0001-1, Bio X Cell) and anti-CD28 (5 μg ml⁻¹; BE0015-1, Bio X Cell) in complete RPMI media with recombinant murine IL-2 (20 ng ml⁻¹; 212-12, Peprotech).

METHODS DETAILS

Mouse blood sampling

Blood was collected from the arterial catheter or by tail bleed. For arterial sampling, a cannula was connected to the vascular access button and mice were allowed to recover from handling-induced stress for at least 30 min. Blood was collected from the cannula directly to a collection tube without handling the mouse. For blood collection in the fasted state, mice were transferred to new cages without food at 9 AM, and blood was collected from 3 PM to 6 PM. Blood was kept on ice for up to 1 h followed by centrifugation (10,000 \times g for 3 min, room temperature) as indicated. Serum was isolated from the supernatant and was extracted by methanol immediately (2.5 μL of serum into 70 μL of ice-cold methanol) or stored in -80°C until further analysis.

Measurement of circulatory turnover flux for nucleosides

All measurements were performed in the fasted state. Mice were transferred to new cages without food at 9 AM. Water was supplied as HydroGels (ClearH₂O). Starting at 2 PM, uniformly ¹⁵N-labeled nucleosides (dissolved in 0.9% NaCl) were infused into the jugular vein. For efficiency, one purine tracer and one pyrimidine tracer were infused simultaneously into each mouse. Infusion parameters were summarized in Table S1. Blood was sampled from the arterial catheter 120 min and 150 min after the start of infusion, and by tail bleed after the second arterial sampling. Blood was kept on ice after sampling. For measurement of purines, serum was isolated within 10 min from blood collection by centrifugation (10,000 × g for 3 min) and extracted by methanol (2.5 μL of serum into 70 μL of ice-cold methanol).

Isotope tracing in cultured mouse CD8⁺ T cells

Procedures were adapted from Shen et al.⁶⁰ Isotope tracing in T cells was performed with [U-¹³C]serine (30 mg L⁻¹; CLM-1574, Cambridge Isotope Laboratories, Inc.) and [U-¹⁵N]inosine tracers (2 μM; NLM-4264, Cambridge Isotope Laboratories, Inc.), in RPMI-1640 medium (prepared with R8999-15, USBiological, with correct supplementation; pH 7.4) with 10% dialyzed FBS (F0392, Sigma), 100 U ml⁻¹ penicillin, 100 μg ml⁻¹ streptomycin and 55 μM 2-mercaptoethanol. 24 hours after isolation, T cells were pelleted, washed and resuspended at 1e6 cells ml⁻¹ in tracing medium, either with IL-7 for naïve cells or IL-2 for activated cells, and cultured for 12 h before metabolite extraction. As inosine is rapidly consumed by the T cells, to maintain the 2 μM starting [U-¹⁵N]inosine concentration, the cultures were spiked every 90 minutes with inosine (1 μM for naïve and 1.5 μM for activated, as the activated cells consume inosine faster as measured by LC-MS of the culture media).

Mouse infusion

Unless otherwise indicated, infusions were performed from 7 PM to 8 AM of the following day to trace purine ring turnover. Mice were single-housed with food and water provided *ad libitum*. Infusion parameters are summarized in Table S1. At the end of infusion, blood was collected by tail bleed, and mice were euthanized by cervical dislocation. Spleens, tumor-draining inguinal lymph nodes, and tumors were cut in half, with one half for cell sorting and the other half for snap-freezing. To snap-freeze, tissues were wrapped in foils, clamped by a Wollenberger clamp precooled in liquid N₂, and dropped in liquid N₂.

Formate and methanol dosing in monkeys

Restrained, non-sedated adult male monkeys (Hainan Jingang Biotech) were fasted overnight and re-fed 4 hours after dosing. Methanol or sodium formate was dissolved into saline and filtered through a 0.22 μm filter prior to administration. Intravenous doses were delivered as a bolus injection into a peripheral vein, while oral doses were delivered via nasogastric tube. At the indicated times, approximately 0.5 mL of whole blood was collected into potassium-EDTA tubes and rapidly processed into plasma, which was stored at -80°C until analysis.

Magnetic activated cell sorting and metabolite extraction

Procedures were adapted from Reinfeld et al.¹⁰ Spleens, left inguinal lymph nodes and tumors were cut into halves, and one half was used for cell sorting. Single-cell suspensions of splenocytes were prepared by manual disruption with a syringe plunger and passage through 70 μm cell strainers into PBS. Lymph nodes were disrupted by frosted glass slides and passed through 70 μm cell strainers with PBS. Tumors were chopped and digested in 5 mL of PBS with 435 U/mL DNase (Sigma-Aldrich, D5025) and 218 U/mL collagenase (Sigma-Aldrich, C2674) at 37°C for up to 1 h on a shaker set at 200 rpm. The digested tumor cells were passed through 70 μm cell strainers into PBS. Cell suspensions from tumors, spleens, and lymph nodes were then fractionated using CD8 (TIL) microbeads (Miltenyi Biotec, 130-116-478) according to the manufacturer's instructions. Briefly, cells were resuspended in 10 μL of microbeads and 90 μL of MACS buffer (0.5% BSA + 2 mM EDTA in PBS) per 10⁷ cells at 4°C for 15 min. The magnetically labeled cells were loaded on LS columns (Miltenyi Biotec, 130-042-401) which were secured on Miltenyi MidiMACS Separators. Columns were washed twice, each time with 3 mL of MACS buffer to allow unlabeled cells to pass (collected as the CD8⁻ fraction). Columns were then removed from the MidiMACS Separators and flushed with 3 mL MACS buffer to collect the CD8⁺ fraction. The fractionated cells were resuspended in 1 mL of MACS buffer, with 20 μL used for cell counting, 900 μL for metabolic extraction, and all the remaining (~80 μL) stained for flow cytometry.

To extract metabolites, cells were mixed with ice-cold acetonitrile:methanol:water (2:2:1, supplemented with 0.5 vol% formic acid which increases triphosphate yield⁶¹). 20 μL of extraction buffer per 10⁶ cells, or a total of 70 μL, whichever is more, was used. Extracts were vortexed for 10 s, and neutralized by NH₄HCO₃ (15% in water, 8.8% vol/vol of extraction buffer was used). Neutralized extracts were vortexed for 10 s again, kept on dry ice for 1h, and centrifuged (19,930 × g, 30 min at 4°C). Supernatants were collected and kept at -80°C until analysis.

Flow cytometry analysis

Single-cell suspensions from tumors, spleens, or lymph nodes were incubated in Fc block (BD Biosciences, 553142, vol/vol 1/50) at room temperature for 10 min, stained for surface markers on ice for 30 min, washed once with staining buffer (PBS + 2% FBS), and resuspended in staining buffer for analysis on FACSymphony A3 or LSR II (BD Biosciences). The anti-mouse antibodies used were: CD4 (APC-Cy7, 1:100, clone RM4-5, BD Biosciences, 565650; BUV805, 1:400, clone GK 1.5, BD Biosciences, 612900), CD8a (Alexa Fluor 700, 1:400, clone 53-6.7, Biolegend, 100730), CD8b (Alexa Fluor 488, 1:250, clone YTS156.7.7, Biolegend, 126628), CD45.2

(eFluor 450, 1:100, clone 104, Thermo Fisher, 48-0454-82; APC-Cy7, 1:400, clone 104, Biolegend, 109824), CD62L (PE-Cy7, 1:400, clone MEL-14, BD Biosciences, 560516), CD69 (PE-CF594, 1:400, clone H1.2F3, BD Biosciences, 562455). One of the following viability dyes was used according to the manufacturer's instructions: Live/Dead Aqua (Thermo Fisher, L34966), DAPI (1:1000, Thermo Fisher, 62248), or propidium iodide (Thermo Fisher, R37169). All flow cytometry data was analyzed with FCS Express 7.12 (*De Novo Software*). The following gating strategy was used: FSC-A/SSC-A lymphocyte gate, FSC-A/FSC-H singlet gate, live CD45.2⁺ cells, CD8⁺ (using CD4 versus CD8), naive (CD62L⁺) or activated (CD69⁺). Representative purities by magnetic activated cell sorting are shown in [Figures S2A and S2B](#).

Tissue metabolite extraction

Eppendorf tubes and ceramic beads were precooled on dry ice. Tissues were transferred to Eppendorf tubes and disrupted by cryo-mill (Retsch). About 10 mg of homogenized tissue powder was weighed and extracted by ice-cold acetonitrile:methanol:water (2:2:1, supplemented with 0.5 vol% formic acid). Extracts were vortexed for 10 s, and neutralized by NH₄HCO₃ (15% in water, 8.8% vol/vol of extraction buffer was used). Neutralized extracts were vortexed for 10 s again, kept on dry ice for 1 h, and centrifuged (19,930 × g, 30 min at 4°C). Supernatants were collected and kept at –80°C until analysis.

Formate derivatization

Analysis of formate is challenging due to unlabeled formate in procedure blanks, and this value was subtracted from the observed levels in experimental samples. Given the importance of this measurement, both GC-MS and LC-MS were used.

To measure [¹³C] or [D]formate concentration only (not unlabeled formate) in serum samples, an LC-MS-compatible derivatization method for carboxylic acids (adapted from Zeng et al.⁶²) was used. It enabled amide bond formation between carboxylic acid and 3-nitrophenylhydrazine (3-NPH) with coupling reagent 1-ethyl-3-(3-(dimethylamino)propyl)carbodiimide (EDC). 2 μL of serum was added to 40 μL of derivatization reagent (25 mM 3-NPH, 12 mM EDC, 2.4 vol % pyridine, in methanol) and was incubated on ice for 1 h. Samples were spun (19,930 × g, 20 min at 4°C), and the reaction was quenched by adding 10 μL of supernatant to 90 μL of sodium propionate (5 mM in water). The mixture was incubated on ice for 10 min and centrifuged (19,930 × g, 10 min at 4°C) again. Supernatants were collected and kept at 4°C until analysis. [¹³C] or [D]formate concentration was extrapolated from standard curves or internal [¹³C, D]formate standard after natural abundance correction.

To measure both unlabeled and ¹³C-labeled formate in serum samples, a GC-MS-compatible derivatization method (adapted from Meiser et al.³⁶) was used. In short, formate was converted to benzyl formate by reaction with benzyl alcohol and chloromethyl chloroformate (CMCF). A reaction mixture was prepared by adding 2.5 μL of benzyl alcohol and 20 μL of pyridine into an Eppendorf tube. Then 10 μL of serum was added and mixed by pipetting. To initiate the reaction, 5 μL of CMCF was added, and tubes were quickly capped and vortexed for 15 s. The procedure must be performed in fume hoods as gaseous HCl is generated. The mixture was allowed to sit at room temperature for 20 min and then diluted by 100 μL of water and 100 μL of methyl *t*-butyl ether (MTBE). Samples were vortexed for 5 s, spun (19,930 × g, 10 min at 4°C), and the organic layer was transferred to glass vials. Vials were kept at room temperature until analysis. By GC-MS, a trace amount of benzyl formate was observed in benzyl alcohol (from various vendors) directly diluted in MTBE, which is likely an impurity from the reagent and contributes to the formate background in procedure blanks (~30 μM). To subtract the background, standard curves with at least three procedure blanks were used to extrapolate formate concentration after natural isotope correction.

LC-MS method

Metabolites were separated by hydrophilic interaction liquid chromatography (HILIC) with an XBridge BEH amide column (2.1 mm × 150 mm, 2.5 μm particle size; Waters, 186006724). The column temperature was set at 25°C. Solvent A was 95 vol% H₂O 5 vol% acetonitrile (with 20 mM ammonium acetate, 20 mM ammonium hydroxide, pH 9.4). Solvent B was acetonitrile. Flow rate was 0.15 mL/min. The LC gradient was: 0–2 min, 90% B; 3–7 min, 75% B; 8–9 min, 70% B; 10–12 min, 50% B; 12–14 min, 25% B; 16–20.5 min, 0.5% B; 21–25 min, 90%.

MS analysis was performed on Thermo Fisher's Q Exactive Plus (QE+) Hybrid Quadrupole-Orbitrap, Orbitrap Exploris 240, or Orbitrap Exploris 480 mass spectrometer. Full scan was performed in negative mode, at the *m/z* of 70–1000. The automatic gain control (AGC) target was 3e6 on QE+ and 1000% on Exploris 240/480. The maximum injection time was 500 ms on QE+ and Exploris 480, and 200 ms on Exploris 240. The orbitrap resolution was 140,000 on QE+, and 180,000 on Exploris 240/480. Selected ion monitoring (SIM) was performed for ATP in negative mode at the retention time of 13–15 min, *m/z* 505–515, AGC target 1e6 (QE+) or 1000% (Exploris 240/480), maximum injection time 500 ms, and orbitrap resolution 140,000 (QE+) or 240,000 (Exploris 240), or 480,000 (Exploris 480).

Derivatized formate (by reaction with 3-NPH) was analyzed by QE+. LC separation was done by a reversed-phase method, with an Acquity UPLC BEH C18 column (2.1 mm × 100 mm, 1.7 μm particle size, 130 Å pore size; Waters, 186002352) using a gradient of solvent A (water) and solvent B (methanol): 0–1 min, 10% B; 5 min, 30% B; 7–10 min, 100% B; 10.5–18 min, 10% B. Flow rate was 0.2 mL/min. Selective ion monitoring was done in negative mode with *m/z* 178 to 186, AGC target 3e6, and maximum injection time 500 ms.

GC-MS method

To analyze formate (derivatized to benzyl formate), 0.5 μL of sample was loaded on Agilent's 7250 GC/Q-TOF in splitless injection mode. The injection port was set at 250°C. GC separation was performed on a VF-WAXms fused silica column (30 m \times 0.25 mm, 0.5 μm film thickness, Agilent, CP9222), with the oven temperature programmed as follows: initiation at 56°C and hold for 3 min, then ramped to 220°C (ramp rate 30°C/min) and hold for 5 min. Helium was used as the carrier gas at a constant flow rate of 1.1 mL/min. Electron ionization was set at the low energy mode (15 eV), and full scan was performed at m/z 50–500.

To analyze methanol, 50 μL of plasma was mixed with 150 μL of N-methyl-2-pyrrolidone containing acetonitrile as an internal standard (final concentration = 26 $\mu\text{g}/\text{mL}$) in glass vials. Vials were sampled with an Agilent 7697A Headspace Sampler and analyzed by a 7890B GC system coupled to a 5977B mass spectrometer. The column was an Agilent DB-WAX Ultra Inert GC column (30 m \times 0.25 mm \times 0.25 μm) using helium as a mobile phase at a flow rate of 1 mL/min. The temperature gradient was as follows: 30°C, 5 minutes; ramp to 230°C at a rate of 120°C/minute; hold for 3 minutes. Additional GC parameters: vial equilibration, 5 minutes; solvent delay, 1.6 minutes; headspace oven temp, 60°C; headspace loop temp, 120°C; MS transfer line temp, 280°C. Analytes were ionized by electron ionization and detected as the molecular ions. Additional MS parameters: source temp, 230°C; quadrupole temp, 150°C. Concentrations were determined using external standard curves prepared in plasma from untreated monkeys.

Formate measurement by ion chromatography

To measure formate in the plasma from monkeys, 75 μL of plasma was diluted in 150 μL of acetonitrile and centrifuged (14,000 \times g, 10 minutes). 150 μL of supernatant was diluted into 300 μL of water, and 25 μL was injected into a Dionex ICS-5000+ IC system using an IonPac AS18 RFIC column (250 mm \times 4 mm) with an IonPac AG11-HC RFIC guard column (250 mm \times 4 mm). The mobile phase was water with potassium hydroxide generated by a Dionex EGC 500 KOH cartridge. The KOH gradient was: 0 to 15 minutes, 8 mM; 15 to 15.1 minutes, ramp to 50 mM; 15.1 to 20 minutes, 50 mM; 20 to 20.1 minutes, drop to 8 mM; 20.1 to 30 minutes 8 mM. Flow rate was 1 mL/minute. Column temperature was 30°C. Analytes were detected by electron capture. Concentrations were determined using external standard curves prepared in plasma from untreated monkeys.

PD-1 efficacy with nutrient supplementation

Anti-tumor efficacy experiments were performed at Charles River Laboratories. Female C57BL/6 mice were used which were 8–12 weeks old at the date of tumor initiation. Water and Rodent NIH-31M Auto chow (Ziegler Feed) was provided *ad libitum*. To initiate tumors, 5×10^5 MC38 cells in 1 mL PBS were injected subcutaneously on the flank of each mouse. When the average tumor volume reached 80–120 mm^3 , mice were randomized into different groups and were treated with anti-PD-1 (5 mg/kg, clone RMP1-14, low endotoxin, ichorbio IHC1132) or isotype control Rat IgG2a (5 mg/kg, clone 2A3, BioXcell BE0089) twice per week for two weeks. Nutrient supplementation started from the first dose of antibody treatment and lasted until experimental endpoint. To supplement formate, sodium formate (2% w/v) was provided in the drinking water. To supplement formate via methanol, 2 g/kg of methanol (25% v/v in saline, dosing volume 10 mL/kg) was administered via daily oral gavage. To supplement inosine, 0.9 g/kg of inosine (90 mg/mL suspension in PBS, dosing volume 10 mL/kg) was administered twice per day (12 h intervals) via oral gavage. For MC38 rechallenge, 5×10^5 MC38 cells were injected subcutaneously on the opposite flank of tumor-free mice from anti-PD-1 \pm methanol treatment or age-matched female C57BL/6 control mice. No antibody or methanol was administered. Tumor volumes were measured twice per week.

Data analysis

Raw mass spectrometry data were converted to.mzXML format by MSConvert (ProteoWizard).⁶³ Pick-peaking was done on EI Maven (v0.8.0, Elucidata).⁶⁴ Natural isotope abundance was corrected by the 'accucor'⁶⁵ package on R for all metabolites except ATP, whose $^{13}\text{C}_2$ ($-\text{H}^+$ 507.9952 m/z) isotopomer is partially resolved from $^{18}\text{O}_1$ ($-\text{H}^+$ 507.9927 m/z). To address this, an algorithm (optCorr,⁵⁸ available at https://github.com/xxing9703/optCorr_script or via <https://doi.org/10.5281/zenodo.10976652>) was developed. It accounts for the contribution from unresolved or partially resolved peaks to the observed peak top (e.g., the contribution from $^{18}\text{O}_1$ to the $^{13}\text{C}_2$ peak top) by simulating MS profiles. Natural abundance correction for ATP was done by optCorr.

Circulatory turnover flux (F_{circ}) of nucleosides was determined by the same method as previously described.⁴² F_{circ} was calculated by

$$F_{\text{circ}} = \frac{1 - L}{L} R \quad (\text{Equation 2})$$

where L is the fraction of labeled nucleoside in arterial serum, and R is the rate at which such nucleoside was infused.

The fraction of newly synthesized ATP was calculated by the fractional purine ring carbon atom labeling from infusing [^{13}C] serine. Such labeling comes from both labeled glycine and labeled 1C units. The resulting total ATP carbon atom labeling is given by $\sum_i i \times L_{\text{ATP}, M+i}$ (maximum 4 carbon atoms if all serine and glycine were labeled) with the M+3 and M+4 forms undetectable (as

expected from the minimally perturbative serine infusion). Given actual serine and glycine labeling, the possible total ATP carbon atom labeling (if all ATP were new) is given by $2 \times L_{gly,M+2} + 2 \times (L_{ser,M+1} + L_{ser,M+3})$. The newly synthesized ATP fraction is the ratio of these:

$$f_{de\ novo} = \frac{L_{ATP,M+2} + \frac{1}{2}L_{ATP,M+1}}{L_{ser,M+1} + L_{ser,M+3} + L_{gly,M+2}} \quad (\text{Equation 3})$$

In isolated cells, serine and glycine labeling was diluted during sample preparation, so labeling measured in clamped bulk tissues was used instead.

The fraction of ATP with its purine ring from circulating inosine $f_{inosine}$ was calculated by normalizing the ATP labeling to serum allantoin as a surrogate for inosine.

$$f_{inosine} = \frac{L_{ATP,M+4}}{L_{allantoin,serum}} \quad (\text{Equation 4})$$

For [U-¹⁵N]adenosine infusion, tissue ATP labeling was normalized to arterial adenosine enrichment $L_{adenosine,serum}$ measured independently in double catheterized mice.

$$f_{adenosine} = \frac{L_{ATP,M+5} + L_{ATP,M+4}}{L_{adenosine,serum}} \quad (\text{Equation 5})$$

Note that the M+4 ATP (a relatively small fraction) can come from M+5 ATP via the purine nucleotide cycle or from circulating inosine labeled by adenosine. No correction was made to subtract adenosine→inosine→ATP contributions.

The direct contribution to the tumor 1C pool was determined by a linear algebra strategy previously described for other metabolites.⁴² Both serine and formate from circulation can label the 1C pool for purine synthesis, and each can label the other. The goal is to figure out the direct 1C source correcting for the indirect routes (e.g., circulating formate → circulating serine → purine 1C). This is important for ensuring that there is a direct 1C contribution from circulating formate.

In either [U-¹³C]serine or ¹³C-formate infusion, the fraction of labeled 1C pool in tissues L_{1C} can be accounted for by the sum of direct contribution of circulating serine and formate (f_{ser} and f_{for}), and serine/formate labeling. For serine, both M+1 and M+3 can contribute to labeled 1C units, so we call $L_{serum,ser1C} = L_{serum,ser,M+1} + L_{serum,ser,M+3}$.

$$L_{1C} = f_{ser} \cdot L_{serum,ser1C} + f_{for} \cdot L_{for} \quad (\text{Equation 6})$$

In [U-¹³C]serine infusion, define $L_{ser→for}$ as the fraction of circulating formate from circulating serine:

$$L_{ser→for} = \frac{L_{for}}{L_{serum,ser1C}} \quad (\text{Equation 7})$$

Thus, Equation 6 becomes

$$L_{1C} = f_{ser} \cdot L_{serum,ser1C} + f_{for} \cdot L_{serum,ser1C} \cdot L_{ser→for} \quad (\text{Equation 8})$$

Similarly, in ¹³C-formate infusion,

$$L_{1C} = f_{ser} \cdot L_{serum,for} \cdot L_{for→ser} + f_{for} \cdot L_{serum,for} \quad (\text{Equation 9})$$

Substituting Equations 8 and 9 into Equation 1, and rearranging into matrix form gives:

$$\begin{pmatrix} 1 & f_{ser→for} \\ f_{for→ser} & 1 \end{pmatrix} \begin{pmatrix} f_{ser} \\ f_{for} \end{pmatrix} f_{de\ novo} = \begin{pmatrix} L_{1C←ser} \\ L_{1C←for} \end{pmatrix} \quad (\text{Equation 10})$$

$$L_{1C←ser} = \frac{0.5 \cdot L_{ATP,M+1} \text{ (serine infusion)}}{L_{ser,M+1} + L_{ser,M+3}} \quad (\text{Equation 11})$$

$$L_{1C←for} = \frac{0.5 \cdot L_{ATP,M+1} \text{ (formate infusion)}}{L_{for}} \quad (\text{Equation 12})$$

f_{ser} and f_{for} were calculated by fitting experimental data with Equations 10–12, and errors were determined by bootstrapping.

To account for tumor serine which is not derived from circulation (e.g., *de novo* synthesis), we first calculated its fraction $L_{ser,noncirc}$ by comparing the average carbon-atom labeling for serine in tumors and serum.

$$L_{ser,noncirc} = 1 - \frac{\sum_{i=1}^3 i \cdot L_{tumor,ser,M+i}}{\sum_{i=1}^3 i \cdot L_{serum,ser,M+i}} \quad (\text{Equation 13})$$

Its contribution to tumor's 1C pool $f_{ser,noncirc}$ was calculated by

$$f_{ser,noncirc} = f_{ser} \frac{L_{noncirc}}{1 - L_{noncirc}} \quad (\text{Equation 14})$$

And errors were propagated by standard error propagation methods.

To determine the 1C pool labeling in isolated cells from perturbative ^{13}C -formate infusions, we used the ratio of M+1 and M+2 fractions for ATP. The fraction of M+2 ATP is given by

$$L_{ATP,M+2} = f_{de\ novo} (L_{1C})^2 \quad (\text{Equation 15})$$

Solving for L_{1C} from [Equations 1](#) and [15](#) gives

$$L_{1C} = \frac{L_{ATP,M+2}}{L_{ATP,M+2} + 0.5 \cdot L_{ATP,M+1}} \quad (\text{Equation 16})$$

QUANTIFICATION AND STATISTICAL ANALYSIS

Statistical tests were indicated in figure legends, with $p < 0.05$ used to determine statistical significance. For isotope tracing experiments with cell sorting, samples with cell purity <90% (determined by flow cytometry) were excluded from analysis.